

UC San Diego

UC San Diego Previously Published Works

Title

Regional-Scale Lithospheric Recycling on Venus via Peel-Back Delamination

Permalink

<https://escholarship.org/uc/item/2b15f06b>

Authors

Adams, Andrea C
Stegman, David R
Smrekar, Suzanne E
[et al.](#)

Publication Date

2022-10-06

DOI

10.1029/2022JE007460

Data Availability

The data associated with this publication are available at:
<https://doi.org/10.5281/zenodo.6819751>

Peer reviewed

Regional-Scale Lithospheric Recycling on Venus via Peel-Back Delamination

A. C. Adams¹, D. R. Stegman¹, S. E. Smrekar², P. J. Tackley³

¹Institute of Geophysics and Planetary Physics, Scripps Institution of Oceanography, University of
California, San Diego, CA, USA

²Jet Propulsion Laboratory, California Institute of Technology, Pasadena, CA, USA

³Institute of Geophysics, Department of Earth Sciences, ETH Zürich, Zürich, Switzerland

Key Points:

- Dense lithospheric mantle on Venus can decouple from crust at the surface and be recycled into the interior
- A regime diagram provides the conditions when peel-back delamination is favored over stagnant-lid despite having net-positive plate buoyancy
- Peel-back delamination may be a source of tectonic/volcanic resurfacing within the framework of regional equilibrium resurfacing

Corresponding author: Andrea Adams, aca009@ucsd.edu

Abstract

We currently have a limited understanding of the tectonic framework that governs Venus. Schubert and Sandwell (1995) identified over 10,000 km of possible subduction sites at both coronae and chasmata rift zones. Previous numerical and experimental studies have shown the viability of regional-scale lithospheric recycling via plume-lithosphere interactions at coronae, yet little work has been done to study the possibility of resurfacing initiated at Venusian rift zones. We created 2D numerical models to test if and how regional-scale resurfacing could be initiated at a lateral lithospheric discontinuity. We observed several instances of peel-back delamination - a form of lithospheric recycling in which the dense lithospheric mantle decouples and peels away from the weak, initially 30 km-thick crust, leaving behind a hot, thinned layer of crust at the surface. Delamination initiation is driven by the negative buoyancy of the lithospheric mantle and is resisted by the coupling of the plate across the Moho, the significant positive buoyancy of the crust arising from a range of crustal densities, and the viscous strength of the plate. Initial plate bending promotes yielding and weakening in the crust, which is crucial to allow decoupling of the crust and lithospheric mantle. When there is sufficient excess negative buoyancy in the lithospheric mantle, both positively and negatively buoyant plates may undergo delamination. Following a delamination event, the emplacement of hot, buoyant asthenosphere beneath the crust may have consequences for regional-scale volcanism and local tectonic deformation on Venus within the context of the regional equilibrium resurfacing hypothesis.

Plain Language Summary

The tectonic forces that have shaped Venus' surface over time are currently not well understood. Over 10,000 km of possible subduction sites have been identified on Venus, many of which are located near groupings of rift-zone trenches called chasmata. Until now, no studies have tested the viability of subduction initiation at a rift zone on Venus. Here, we created 2D numerical models to determine if and how regional-scale lithospheric recycling events could be initiated at a Venusian rift zone. We observed several cases of a tectonic regime called peel-back delamination, which occurs when dense lithospheric mantle decouples from the crust and peels away, leaving behind a hot, thinned layer of crust at the surface. Delamination initiation is driven by the negative buoyancy of the sub-crustal lithospheric mantle, and is inhibited by the coupling of the plate across the

47 Moho, the positive compositional buoyancy of the crust, and the strength of the plate.
 48 Unlike subduction, both positively and negatively buoyant plates may undergo delam-
 49 ination if there is sufficient negative buoyancy in the lithospheric mantle. Following a
 50 delamination event, the emplacement of hot, buoyant asthenosphere beneath the crust
 51 may have consequences for localized volcanism and regional-scale tectonic deformation
 52 on Venus.

53 **1 Introduction**

54 We currently lack an understanding of the global tectonic and convective frame-
 55 work that has governed Venus throughout its evolution. On Earth, resurfacing occurs
 56 via plate tectonics, where new crust is formed at mid-ocean ridges and old lithosphere
 57 is continuously recycled at subduction zones. Despite being Earth's closest neighbor in
 58 the solar system and having similarities in size and composition, Venus shows no evidence
 59 of Earth-like plate tectonics (Phillips & Hansen, 1994; Solomon et al., 1992). Since NASA's
 60 Magellan mission in the early 1990s, two key observations related to impact craters have
 61 guided our insight into how the surface of Venus may have evolved over time: approx-
 62 imately 975 total craters suggest a relatively young surface age (250-750 Myr) (Feuvre
 63 & Wieczorek, 2011; McKinnon et al., 1997; Schaber et al., 1992; Turcotte, 1993) and the
 64 crater population has a near spatially random distribution (Phillips et al., 1992; Riedel
 65 et al., 2021; Strom et al., 1994). In the decades since Magellan, these observations have
 66 divided ideas about Venus' surface evolution into two hypotheses: (1) the catastrophic/episodic
 67 resurfacing hypothesis and (2) the regional equilibrium resurfacing hypothesis.

68 The catastrophic resurfacing (CR) model describes a tectonic regime where the cool-
 69 ing and thickening of Venus' lithosphere is interrupted by at least one, but perhaps mul-
 70 tiple global-scale overturns over the last 4.5 billion years (Parmentier & Hess, 1992; Tur-
 71 cotte, 1993, 1995; Turcotte et al., 1999). These events are thought to occur over rela-
 72 tively short geologic timescales (<100 Myr) and are followed by a period of resurfacing
 73 (Namiki & Solomon, 1994; Strom et al., 1994). This theory rose in popularity because
 74 the post-overturn uniform surface age is a simple explanation for the spatially random
 75 crater distribution on Venus. The young surface age implies that the most recent over-
 76 turn event happened in the last 250-750 Myr, and the CR hypothesis attributes the mostly
 77 unmodified crater population to low levels of tectonic or volcanic activity during the fol-

78 lowing quiescent period (Herrick, 1994; Schaber et al., 1992). Convection models from
 79 previous studies support the CR hypothesis by producing cyclic global overturn events
 80 under certain conditions (Armann & Tackley, 2012; Crameri & Tackley, 2016; Moresi &
 81 Solomatov, 1998; Reese et al., 1999; Rolf et al., 2018; Weller & Kiefer, 2020; Uppalap-
 82 ati et al., 2020).

83 Despite being compatible with first-order cratering constraints, the CR model is
 84 not unequivocally supported by all models and observations. The offset between the cen-
 85 ter of mass and center of figure (CM-CF) of Venus is a measurable quantity that can sig-
 86 nify large-scale density anomalies in a planet’s surface (topography) and interior (ther-
 87 mal anomalies). King (2018) analyzed the immediate and long-term effects of one or more
 88 global overturns on the calculated CM-CF offset in models of Venus. The calculated off-
 89 sets were significantly larger than the the observed CM-CF offset, indicating the observed
 90 offset is incompatible with a global resurfacing event (King, 2018). Furthermore, the CR
 91 hypothesis can be rejected because a uniform surface age contradicts observations that
 92 different stages of impact crater degradation are associated with different geological re-
 93 gions on Venus (Basilevsky & Head, 2002; Herrick & Rumpf, 2011; Izenberg et al., 1994).
 94 Combined with the association between crater density and geology, the three average model
 95 surface age (AMSA) provinces dividing the surface of Venus into relative ages (old, in-
 96 termediate, and young) (Hansen & Young, 2007; Phillips & Izenberg, 1995), point to-
 97 ward a more complex resurfacing history.

98 The competing idea to explain Venus’s unique style of resurfacing is the regional
 99 equilibrium resurfacing (RER) hypothesis. It suggests Venus’ crater population is a bal-
 100 ance between steady-state crater formation and the removal of craters by tectonic or vol-
 101 canic processes occurring at different rates regionally (Phillips et al., 1991, 1992). Al-
 102 though some early statistical analyses could not reconcile the observed crater popula-
 103 tion with frequent, smaller resurfacing events (Bullock et al., 1993; Strom et al., 1994),
 104 more recent Monte Carlo experiments found that the uniform crater distribution and num-
 105 ber of modified craters can be explained by regional equilibrium resurfacing (Bjornes
 106 et al., 2012; O’Rourke et al., 2014). The RER model may also be compatible with both
 107 the observed CM-CF offset for Venus (King, 2018) as well as the association with crater
 108 population and geology (Phillips & Izenberg, 1995). The RER hypothesis is further sup-
 109 ported by evidence of regional-scale volcanic activity from thermal emissivity anoma-
 110 lies observed at volcanoes (Shalygin et al., 2012) and chasma rift zones (Shalygin et al.,

111 2015). Surface emissivity data indicating a lack of chemical weathering at coronae and
112 volcanoes over plume-associated topographic rises also signify geologically-recent volcan-
113 ism on Venus (Smrekar et al., 2010).

114 In addition to volcanic processes, there is evidence that tectonic processes may also
115 drive regional-scale resurfacing events. Sandwell and Schubert (1992) observed that trench-
116 outer rise topography and lithospheric flexure across several of Venus' largest coronae
117 are comparable to various arcuate subduction zones on Earth (Sandwell & Schubert, 1992).
118 This is interpreted as evidence for retrograde subduction which may have initiated due
119 to interactions between the lithosphere and a rising mantle plume. The viability of plume-
120 induced subduction at Venusian coronae has since been studied in both numerical (Gülcher
121 et al., 2020) and laboratory experiments (Davaille et al., 2017) and is the favored model
122 for regional-scale subduction on Venus - in part because the plume provides a mecha-
123 nism to weaken and break the lithosphere. Melt weakening (Gülcher et al., 2020) and
124 loading due to surface volcanism (Sandwell & Schubert, 1992) may cause the lithosphere
125 to break and its edges to sink and migrate radially outward. Plume-induced subduction
126 may be ongoing at present, as evidenced by anomalously-high thermal emissivity at Quet-
127 zalpetlatl corona indicating geologically-recent volcanism (Davaille et al., 2017).

128 Plume-lithosphere interactions are a mechanism to induce weakness in the litho-
129 sphere and facilitate subduction initiation, but subduction itself is primarily driven by
130 the negative buoyancy of the plate. For Venus, subduction and lithospheric recycling may
131 be complicated by the presence of positively-buoyant plates. Large regional variations
132 (and uncertainties) in crust and lithosphere thickness (Anderson & Smrekar, 2006; James
133 et al., 2013) and potentially warmer mantle temperatures with higher degrees of melt-
134 ing and crust formation affect the net buoyancy of the lithosphere and its ability to subduct.
135 In order to better understand the viability of regional-scale tectonic resurfacing, it is im-
136 portant to constrain a range of conditions for which lithospheric recycling may occur on
137 Venus without the added complexities of plume-lithosphere interactions. In addition to
138 coronae, thousands of kilometers of chasmata (Dali and Diana chasmata, Hecate Chasma,
139 Parga Chasma, etc.), or rift zones, are proposed to be possible sites of subduction on Venus
140 (Sandwell & Schubert, 1992; Schubert & Sandwell, 1995). Here, we present 2D numer-
141 ical models of a simplified Venusian chasma rift zone over a range of crust and mantle
142 conditions to identify if and how regional-scale lithospheric recycling can occur without
143 assistance from mantle plume interactions.

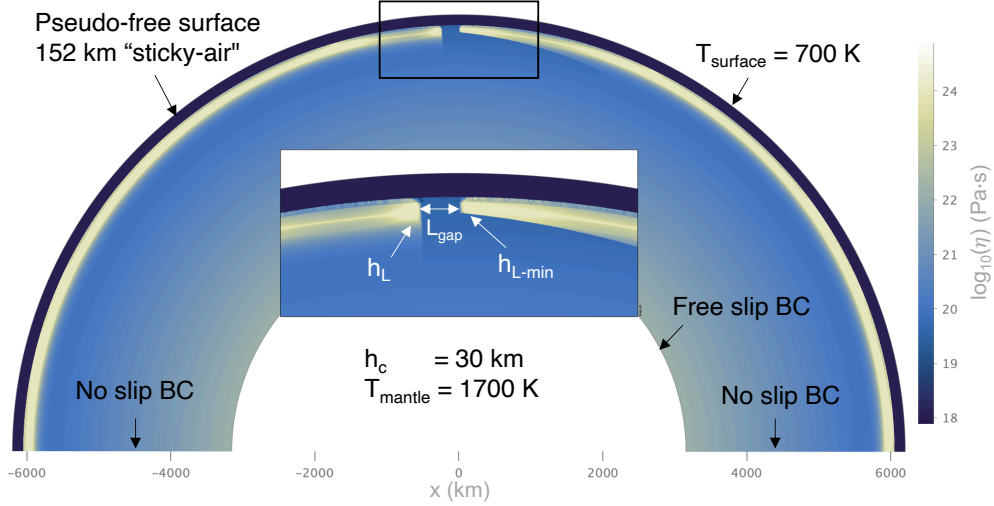


Figure 1. Viscosity field of initial model setup. A gap ($L_{gap} = 250$ km) separates two plate edges with thicknesses $h_L = [200, 250, \text{or } 300]$ km (left) and $h_{L-min} = 100$ km (right). The lithosphere with thickness h_{L-min} gradually thickens to be thickness h_L . The gap represents a simplified rift zone or an area having undergone previous magmatic weakening. The model setup is designed to study buoyancy-driven lithospheric recycling events in the absence of an imposed velocity field or slab perturbation as to be more representative of Venus.

144 2 Methods

145 2.1 Model Setup

146 We performed a series of numerical experiments using StagYY, a finite-volume code
 147 which models solid-state mantle convection by solving the conservation of mass, momen-
 148 tum, and energy equations on a staggered grid (Tackley, 2008; Crameri et al., 2017). We
 149 consider viscous flow of an infinite Prandtl number fluid and assume an incompressible
 150 mantle using the Boussinesq approximation. Composition is tracked using over 13.6 mil-
 151 lion (13694800) tracer particles in a 2048x512 resolution grid space. All visualization was
 152 performed using StagLab (Crameri, 2021).

153 2.2 Initial Condition

154 The model geometry is a two-dimensional 180° spherical annulus (Hernlund & Tack-
 155 ley, 2008). The initial condition consists of a lithosphere with a single discontinuity where
 156 a 250 km-wide gap separates two edges of the lithospheric mantle (Fig. 1). The gap is
 157 filled with relatively warm asthenospheric material. The gap is a simplified representa-
 158 tion of a rift zone or an area where a previous thermal upwelling left behind an area of
 159 magmatically-weakened lithosphere. Rift widths are locally similar to the model gap be-
 160 tween plates. For example, the 10,000 km-long fracture zone of Parga Chasma varies from
 161 90-590 km; the trough is 60-230 km wide and 0.5-2 km deep (Martin et al., 2007). A 30
 162 km-thick layer of basaltic crust (h_c) covers the entire domain including the gap. The plate
 163 to the left of the gap is uniformly thick ($h_L = [200, 250, 300]$ km) and covers an upper
 164 range of lithosphere thicknesses that may be present on Venus (Anderson & Smrekar,
 165 2006). The plate to the right of the gap is thinned at its edge (constant $h_{L-min} = 100$
 166 km) and gradually thickens to h_L . The asymmetry in lithospheric thickness across the
 167 gap may reflect cases of observed asymmetry across Venusian chasmata (Schubert & Sandwell,
 168 1995). We use a mantle potential temperature of 1700 K (Nimmo & McKenzie, 1997;
 169 Shellnutt, 2016) and define lithosphere thickness by the 1600 K isotherm. There is no
 170 initial velocity-field perturbation or pre-existing plate bending to assist the initiation of
 171 plate motion.

172 *2.3 Boundary Conditions*

173 All models employ a pseudo-free-surface upper boundary condition with 152 km
 174 of “sticky-air” which allows for the development of realistic topography and is known
 175 to influence lithosphere dynamics (Cramer et al., 2012). The surface temperature is de-
 176 fined by a 700 K isothermal boundary. We use a free-slip lower boundary and no-slip side-
 177 wall boundary conditions. The no-slip sidewall boundaries simulate the resistance of the
 178 surface to slab pull during potential lithospheric recycling events, which may best rep-
 179 resent an effectively single-plate planet such as Venus. The sidewall boundaries are suf-
 180 ficiently far from the gap so there is no interference with local mantle flow.

181 *2.4 Viscosity*

182 Diffusion creep and plastic failure are assumed to be the only deformation mech-
 183 anisms. Temperature and pressure-dependent viscosity is defined by the Arrhenius law:

$$\eta(T, p) = \eta_0 \cdot \exp \left[\frac{E_a + (1 - z)V_a}{T} - \frac{E_a}{T_0} \right] \quad (1)$$

184 where E_a and V_a are the activation energy and volume, respectively, and the ref-
 185 erence viscosity, η_0 , is 10^{20} Pa·s at zero pressure and 1600 K. An activation energy of
 186 240 kJ/mol was chosen corresponding to a wet olivine rheology. We use an activation
 187 volume of 10^{-7} m³/mol to approximate a pressure- and temperature-dependent viscos-
 188 ity increase of three orders of magnitude over the depth of the mantle. Viscosity vari-
 189 ations in the mantle were restricted to six orders of magnitude with a maximum viscos-
 190 ity of 10^{25} Pa·s and a minimum viscosity of 10^{19} Pa·s. The viscosity of the sticky-air was
 191 10^{18} Pa·s. The maximum viscosity of the lithosphere was controlled separately and var-
 192 ied between three values spanning two orders of magnitude, $\eta_{max} = [10^{23}, 10^{24}, 10^{25}]$
 193 Pa·s (Supplementary Fig. 1).

194 2.5 Yield Strength

195 Plasticity is implemented using the Drucker-Prager criterion based on Byerlee's law
 196 to calculate the pressure-dependent brittle yield stress

$$\tau_{y,brittle} = C + p\mu \quad (2)$$

197 with cohesion, C , confining pressure, p , and friction coefficient, μ . The models described
 198 here all use a surface cohesion of 10 MPa and a friction coefficient of 0.25. The effective
 199 yield stress τ_y is then calculated as the minimum between $\tau_{y,brittle}$ and a constant max-
 200 imum yield stress

$$\tau_y = \min[\tau_{y,brittle}, \tau_{max}] \quad (3)$$

201 which effectively limits the yield stress to a maximum value of τ_{max} at higher pressure
 202 and depth. When stress levels exceed the yield stress, the material strength is reduced
 203 by converting the viscosity into an effective viscosity

$$\eta \begin{cases} \eta = \frac{\tau_{\Pi}}{2\dot{\epsilon}_{\Pi}} & \text{for } \tau < \tau_{yield} \\ \eta_{eff} = \frac{\tau_{yield}}{2\dot{\epsilon}_{\Pi}} & \text{for } \tau \geq \tau_{yield} \end{cases} \quad (4)$$

204 When the yield stress is exceeded, stresses in the lithosphere are redistributed to
 205 accommodate the decrease in material strength. While previous models of global over-
 206 turns on Venus use maximum yield stresses (τ_{max}) near 100 MPa (Armann & Tackley,
 207 2012), we chose to employ a maximum yield stress of 500 MPa. This will give a yield

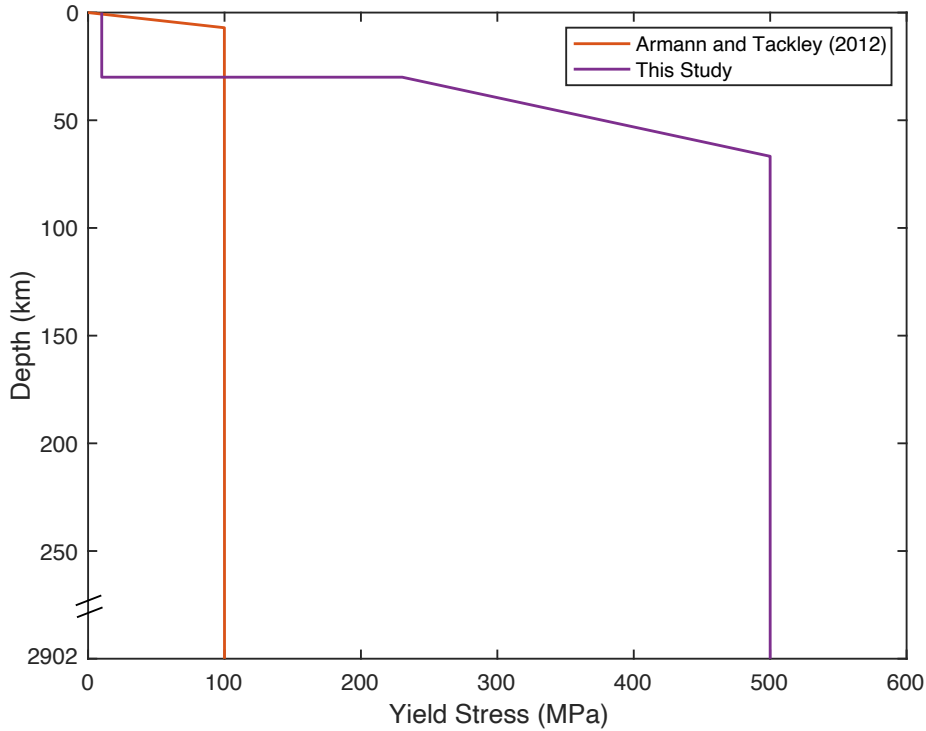


Figure 2. Depth vs yield stress (τ_y) throughout the depth of the mantle. Armann and Tackley (2012) observed vigorous episodic lid overturns when the maximum yield stress (τ_{max}) was 100 MPa. Our models employ weak crust at the surface and a higher maximum yield stress of 500 MPa through the majority of the lithosphere.

208 stress (τ_y) with depth that is stronger throughout the depth of the lithosphere (Fig. 2).
 209 The crust on Venus is suspected to be relatively weak and decoupled from the under-
 210 lying mantle (Arkani-Hamed, 1993; Azuma et al., 2014; Buck, 1992; Ghail, 2015) and
 211 in our models is represented by a material with uniform strength (cohesion of 10 MPa
 212 and friction coefficient approximately zero) which readily yields to tectonic forces (Crameri
 213 & Tackley, 2016).

214 *2.6 Phase Transitions*

215 Tracer particles are used to track compositions within the olivine and basalt/garnet
 216 systems. Compositional phase transitions were implemented as depth-dependent den-
 217 sity contrasts within the two systems relative to the reference density ($\rho_0 = 3300 \text{ kg/m}^3$).

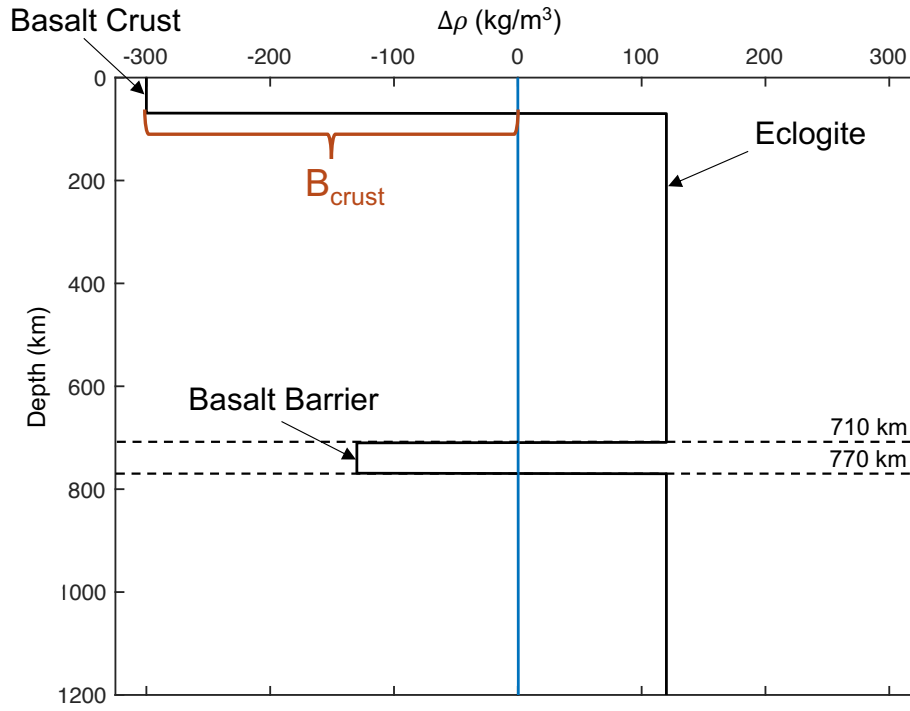


Figure 3. Relative compositional density contrast between basalt-garnet system and olivine system through the depth of the mantle. At the surface, basaltic crust is positively buoyant compared to the reference density (blue line) with $\Delta\rho_c = B_{crust}$ kg/m³ (variable). Eclogite forms and becomes denser than the reference mantle ($\Delta\rho_{ec} = 120$ kg/m³) at 70 km depth. The “basalt barrier” results in a region of positive buoyancy ($\Delta\rho_{bb} = -130$ kg/m³) in the basalt-garnet system between 710 and 770 km depth. Adapted from Ogawa and Yanagisawa (2014).

218 Several Earth-like phase changes were included with depths adjusted to Venus’s lower
 219 gravity (Fig. 3) (Ogawa & Yanagisawa, 2014).

220 At cooler temperatures inside the subducting slab, the postspinel phase boundary
 221 in the olivine system is deflected to deeper depths. Estimates of the value of the post-
 222 spinel Clapyeron slope, γ_{psp} , range from -0.2 to -3.0 MPa/K (Akaogi & Ito, 1993; Fei et
 223 al., 2004; Irifune et al., 1998; Katsura et al., 2003), where more recent estimates fall closer
 224 to zero (Fukao et al., 2009) (see references therein). It is also reported that the effect of
 225 the negative Clapyeron slope is stronger in 2D models than in 3D (Ogawa & Yanagisawa,
 226 2014). A larger Clapyeron slope will deflect the phase boundary to deeper depths and
 227 result in a larger region of positive buoyancy within the slab; conversely, a smaller Clapey-
 228 ron slope may only weakly deflect the postspinel phase boundary. Our models use a value
 229 of $\gamma_{\text{psp}} = -1.0$ MPa/K in order to understand, but not overstate its effect.

230 At 70 km depth, the positively buoyant crust ($\Delta\rho = B_{\text{crust}}$ kg/m³) transforms into
 231 denser eclogite ($\Delta\rho_{\text{ec}} = 120$ kg/m³). Between 710 and 770 km, the garnet-bridgmanite
 232 transition occurs gradually, which results in a region of positive buoyancy ($\Delta\rho_{\text{bb}} = -130$
 233 kg/m³) in the basalt/garnet system relative to bridgmanite. This is referred to as the
 234 garnet trap, or basalt barrier (Davies, 2008), and it coincides with the positively buoy-
 235 ant region within the slab that arises due to deflection of the postspinel boundary. Thus,
 236 there are two separate sources of positive buoyancy within the down-going plate begin-
 237 ning at 710 km depth, which combined have the potential to inhibit slab sinking. Be-
 238 low the garnet trap, the density contrast of the basalt-garnet system returns to $\Delta\rho =$
 239 120 kg/m³.

240 *2.7 Crust Density*

241 The positive compositional buoyancy of the crust counteracts some of the nega-
 242 tive buoyancy of the lithosphere, both of which determine the net buoyancy of the en-
 243 tire plate. In order to explore the effect of crustal buoyancy, we specified the composi-
 244 tional density contrast, $B_{\text{crust}} = \rho_{0,\text{crust}} - \rho_0$, which was prescribed to all crust parti-
 245 cles. An average crust thickness of 30 km (James et al., 2013) was held constant in or-
 246 der to isolate the effects of net crust buoyancy from the effects of variable crust thick-
 247 ness. We vary $B_{\text{crust}} = [-175, -265, -300, -350, -400]$ kg/m³ (Fig. 3). The lowest den-
 248 sity contrast, $B_{\text{crust}} = -175$ kg/m³, represents the compositional density contrast between
 249 olivine and pyroxene-garnet used by Armann and Tackley (2012) in models of global over-

Table 1. Parameters common to all models

Parameter	Description	Value
R	Planetary radius	6052 km
R_{cmb}	Core radius	3150 km
nx	Horizontal cells	2048
nz	Vertical cells	512
g	Gravitational acceleration	8.9 ms^{-2}
ρ_0	Reference density	3300 kgm^{-3}
C_p	Heat capacity at constant pressure	1200.0 J K^{-1}
k	Thermal conductivity	$3 \text{ Wm}^{-1}\text{K}^{-1}$
α	Coefficient of thermal expansion	$3 \times 10^{-5}\text{K}^{-1}$
T_s	Surface temperature	700 K
T_m	Mantle potential temperature	1700 K
η_0	Reference viscosity at $T = 1600 \text{ K}$	$1 \times 10^{20}\text{Pa} \cdot \text{s}$
E_a	Activation energy for wet olivine diffusion	240 kJ/mol
V_a	Activation volume	$10^{-7} \text{ m}^3/\text{mol}$
η_{air}	Air layer viscosity	$1 \times 10^{18}\text{Pa} \cdot \text{s}$
h_{air}	Air layer thickness	152 km
h_c	Crustal thickness	30 km
C_{mantle}	Mantle cohesion	10 MPa
μ_{mantle}	Mantle coefficient of friction	0.25
$C_{weak\ crust}$	Weak crust cohesion	10 MPa
$\mu_{weak\ crust}$	Weak crust coefficient of friction	0.001
γ_{710}	Clapeyron slope of postspinel transition	-1.0 MPaK^{-1}

250 turns; the highest density contrast, $B_{crust} = -400 \text{ kg/m}^3$, represents the expected den-
 251 sity contrast for an Earth-like basaltic crust with $\rho_{crust}=2900 \text{ kg/m}^3$. Ogawa and Yanag-
 252 isawa (2014) predict B_{crust} to be -300 kg/m^3 for crust and mantle compositions of $A_{0.1}B_{0.9}$
 253 and $A_{0.64}B_{0.36}$, respectively, where A is harzburgite and B is garnet and pyroxene (Ogawa
 254 & Yanagisawa, 2014). In addition to compositional density, we consider thermal effects
 255 on density. The crust covering the gap is warmer, and therefore less dense than the crust
 256 covering the plate. A minimum crust thickness of 15 km has been enforced over the en-
 257 tire domain to prevent entrapment of sticky-air particles due to the low viscosity con-
 258 trast between air and mantle material inside the gap.

259 3 Results

260 We investigated lithospheric recycling at a Venusian rift zone for a suite of 42 nu-
 261 merical models with variable crust density, lithosphere thickness, and maximum viscos-
 262 ity (see Table 2). Each model within the suite was identified as in either (I) a peel-back
 263 delamination regime or (II) a stagnant-lid regime. In this section, we discuss the char-
 264 acteristics of the two regimes and the factors affecting their development. Model 23 is

Table 2. Summary of Model Parameters and Outcomes

Model	Crust Density (kg/m ³)	Lithosphere Thickness (km)	Max. Viscosity (Pa·s)	Outcome
1	-175	200	10 ²³	Delamination
2	-175	200	10 ²⁴	Delamination
3	-175	200	10 ²⁵	Delamination
4	-175	250	10 ²³	Delamination
5	-175	250	10 ²⁴	Delamination
6	-175	250	10 ²⁵	Delamination
7	-175	300	10 ²³	Delamination
8	-175	300	10 ²⁴	Delamination
9	-175	300	10 ²⁵	Delamination
10	-265	200	10 ²³	Stagnant-Lid
11	-265	200	10 ²⁴	Stagnant-Lid
12	-265	200	10 ²⁵	Stagnant-Lid
13	-265	250	10 ²³	Delamination
14	-265	250	10 ²⁴	Delamination
15	-265	250	10 ²⁵	Delamination
16	-265	300	10 ²³	Delamination
17	-265	300	10 ²⁴	Delamination
18	-265	300	10 ²⁵	Delamination
19	-300	200	10 ²³	Stagnant-Lid
20	-300	200	10 ²⁴	Stagnant-Lid
21	-300	200	10 ²⁵	Stagnant-Lid
22	-300	250	10 ²³	Delamination
23	-300	250	10 ²⁴	Delamination
24	-300	250	10 ²⁵	Delamination
25	-300	300	10 ²³	Delamination
26	-300	300	10 ²⁴	Delamination
27	-300	300	10 ²⁵	Delamination
28	-350	200	10 ²³	Stagnant-Lid
29	-350	200	10 ²⁴	Stagnant-Lid
30	-350	200	10 ²⁵	Stagnant-Lid
31	-350	250	10 ²³	Delamination
32	-350	250	10 ²⁴	Delamination
33	-350	250	10 ²⁵	Stagnant-Lid
34	-350	300	10 ²³	Delamination
35	-350	300	10 ²⁴	Delamination
36	-350	300	10 ²⁵	Delamination
37	-400	250	10 ²³	Stagnant-Lid
38	-400	250	10 ²⁴	Stagnant-Lid
39	-400	250	10 ²⁵	Stagnant-Lid
40	-400	300	10 ²³	Delamination
41	-400	300	10 ²⁴	Delamination
42	-400	300	10 ²⁵	Delamination

referred to as the reference model due to having intermediate values of crustal buoyancy, plate thickness, and maximum viscosity ($B_{crust} = -300 \text{ kg/m}^3$, $h_L = 250 \text{ km}$, $\eta_{max} = 10^{24} \text{ Pa}\cdot\text{s}$).

3.1 Tectonic Regimes

3.1.1 Regime I: Peel-Back Delamination

Peel-back delamination is a type of lithospheric recycling where the lithospheric mantle detaches and peels away from the lower crust along the Moho. It differs from roll-back subduction because the majority of the basaltic crust remains at the surface as the denser lithospheric mantle is recycled. It also differs from the Rayleigh-Taylor lithospheric dripping style of delamination (Elkins-Tanton, 2007; Göğüş et al., 2017; Houseman & Molnar, 1997; Johnson et al., 2014) because the full depth of the lithospheric mantle is recycled coherently in each event. The following descriptions apply to all observed cases of peel-back delamination.

Delamination initiation is characterized by several distinct stages (Fig. 4). First, the relatively dense sub-crustal lithospheric mantle (SCLM) begins to bend, which induces yielding in the overlying weak crust. As the stress in the crust exceeds its yield strength, the viscosity of the crust is limited to the effective viscosity (Eqn. 4), forming a weak layer near the plate edge which facilitates decoupling of the crust and SCLM (Fig. 4A). As the SCLM continues to bend, buoyant asthenosphere from the gap is wedged between the surface and top of the SCLM. A small amount of buoyant crust (approximately 5 km thick) remains attached to the down-going SCLM, while the majority of crust remains at the surface or as part of a crustal root forming at the hinge of the delaminating plate (Fig. 4D). Once the thin layer of crust on the SCLM reaches the eclogite transition at 70 km depth, it becomes dense relative to the underlying mantle. Simultaneously, the weak zone of yielded crust propagates along the Moho accompanying trench retreat (Fig. 4E-F). As more SCLM progressively detaches from the crust, the crustal root at the trench thickens. When the base of the crustal root reaches 70 km depth, thicker layers of crust undergo the eclogite density inversion (Fig. 4H). The thick layers of eclogite add negative buoyancy to the delaminating plate that help sustain sinking. The thinner lithosphere to the right of the gap never undergoes delamination.

295 After delamination is initiated (Fig. 5A-B), the slab continues to sink until it ap-
 296 proaches the postspinel phase transition at 710 km depth (Fig. 5C). Due to the nega-
 297 tive Clapeyron slope of the postspinel phase change, the cooler SCLM becomes positively
 298 buoyant relative to the surrounding mantle until it reaches sufficient pressure to undergo
 299 the phase transition. The tip of the delaminating slab is deflected in response to encoun-
 300 tering both the postspinel density inversion and resistance from the radial viscosity in-
 301 crease with depth in the mantle (Fig. 5C). As the negatively buoyant eclogite layer reaches
 302 the basalt barrier between 710-770 km depth, it undergoes a separate density inversion
 303 making the basaltic material positively buoyant in relation to the surrounding mantle.
 304 As a result, slab sinking is inhibited by two distinct sources of positive buoyancy in the
 305 down-going plate beginning at 710 km depth (Fig. 6). As the radial viscosity increases
 306 with depth and the slab reaches both density inversions, the plate bends and the slab
 307 tip is deflected to shallower mantle depths (Fig. 5D). When the SCLM and crust ma-
 308 terial eventually sink past the density inversions due to the weight of the slab, they once
 309 again become dense relative to the surrounding mantle. Sinking of the bent plate con-
 310 tinues until thinning and viscous necking at the slab hinge cause the plate to break off
 311 at the surface (Fig. 5E). All delamination models were run until slab break-off occurred
 312 (between 5.32 and 30.6 Myr).

313 *3.1.2 Regime II: Stagnant-Lid*

314 A total of thirteen models were categorized as stagnant-lid (see Table 2). A stagnant-
 315 lid regime is characterized by the absence of delamination or any other significant form
 316 of lithospheric recycling. The warm mantle inside the gap is cooled due to being surrounded
 317 by the colder surface and lithosphere. Over time, the plate edges are smoothed by the
 318 growth of the thermal boundary layer. Model runs were ended when the gap was cooled
 319 enough to effectively fuse the plate edges together across the gap. In some cases when
 320 the maximum viscosity was relatively low ($\eta_{max} = 10^{23}$ Pa·s), the lithospheric mantle
 321 that did not undergo recycling contracted and widened the gap. Ultimately, these plates
 322 were unable to bend and initiate crustal yielding on timescales that would weaken the
 323 crust sufficiently for a delamination interface to form. Despite some initial bending of
 324 the lithospheric mantle, the absence of a weak zone prevented it from delaminating.

325 *3.2 Analysis of Regimes*

326 *3.2.1 Radius of Curvature*

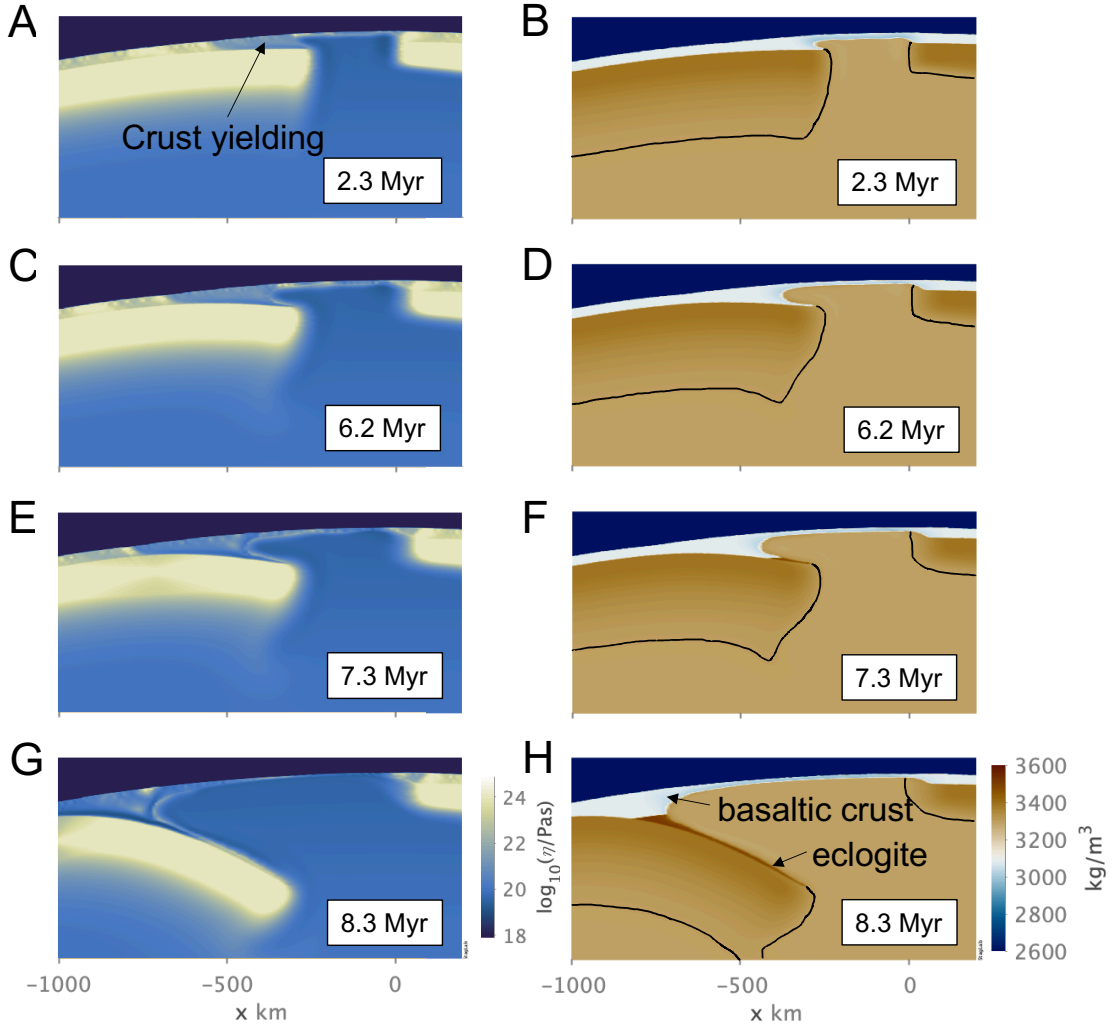


Figure 4. Progression of peel-back delamination initiation shown in the viscosity (left) and density (right) fields of reference model 23 ($B_{crust} = -300 \text{ kg/m}^3$, $h_L = 250 \text{ km}$, $\eta_{max} = 10^{24} \text{ Pa}\cdot\text{s}$). A black line is added to the density field to show the boundary of the lithospheric mantle and asthenosphere defined by the 1600 K isotherm. (A-B) Initial bending of the negatively buoyant lithospheric mantle causes weak crust over plate edge to yield and a small weak zone to form. Crustal yielding appears as a local reduction in viscosity. (C-D) The weak zone propagates as the crust is further yielded and buoyant asthenosphere spreads over the delaminating plate edge. Only a thin layer of crust (5 km) is attached to the delaminating plate. (E-F) Asthenospheric mantle material is wedged deeper into the space between the crust at the surface and the top of the delaminating plate. The crustal root over the delaminating plate hinge thickens and reaches the eclogite transition at 70 km depth, resulting in a density inversion which makes the crust more negatively buoyant than the underlying mantle. (G-H) The delaminating plate continues to detach and peel back from the overlying weak crust layer. Sinking is enhanced by the added negative buoyancy of the eclogitized crust. The thickness of crust attached to the delaminating plate increases as the crustal root deepens and more eclogite is formed. Dark blue layer = sticky-air.

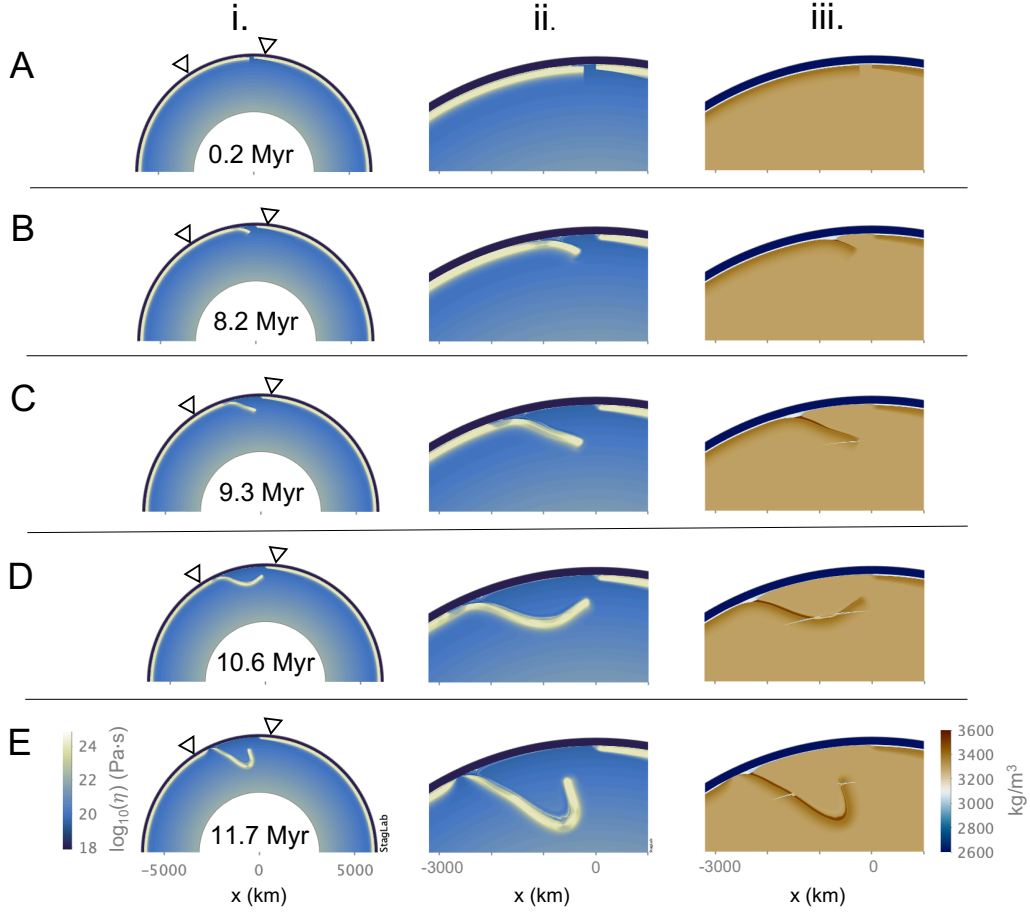


Figure 5. Typical evolution of a peel-back delamination event shown in the (i) full-scale viscosity field, (ii) local viscosity field, and (iii) local density field of reference model 23 ($B_{crust} = -300 \text{ kg/m}^3$, $h_L = 250 \text{ km}$, $\eta_{max} = 10^{24} \text{ Pa}\cdot\text{s}$). (A) A 250 km-wide gap separates the thicker plate edge on the left (h_L) from the 100 km plate edge to the right of the gap. (B) The edge of the thicker plate is bent downward due to the negative buoyancy of the lithospheric mantle. A layer of eclogite is formed in the thin layer of crust still attached to the down-going plate. (C) The lithospheric mantle continues to peel-back from the surface and thicker layers of crust are recycled due to eclogitization of the growing crustal root over the delamination hinge. The slab tip encounters the phase transitions near 710 km depth and (D) is deflected upward. (E) The plate necks and thins at the delamination hinge prior to slab break-off at the surface.

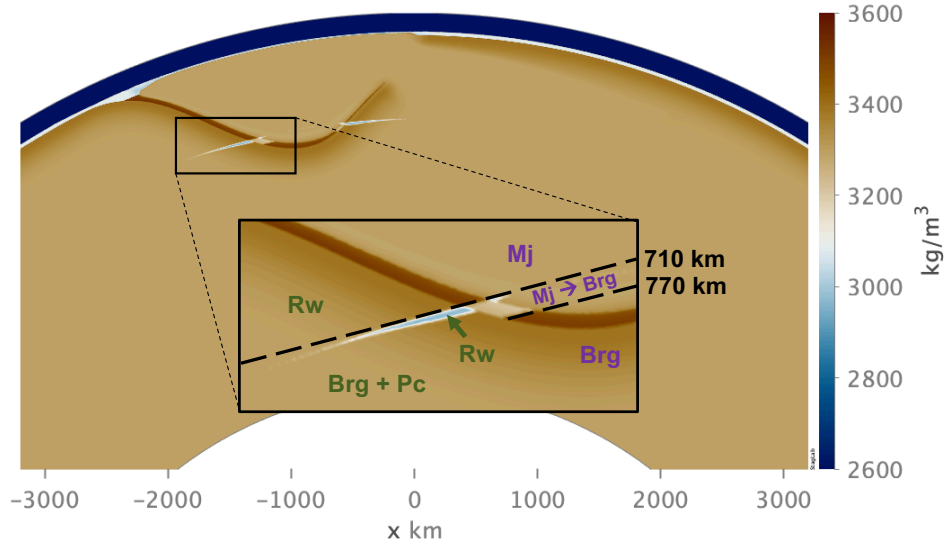


Figure 6. Two separate sources of mid-mantle positive buoyancy within the delaminating slab shown in the density field of the reference model 23. The first is in the olivine system (green text) where the negative Clapeyron slope (-1.0 MPa/K) of the postspinel phase transition deflects the phase boundary to deeper depths within the cold regions of the slab. The transition of ringwoodite (Rw) to bridgmanite (Brg) and periclase (Pc) is delayed, resulting in a thin layer of positive buoyancy within the slab (light blue). The second source of positive buoyancy occurs within the basalt-garnet system (purple text). The basalt barrier is the result of the gradual transition of majorite garnet (Mj) to bridgmanite over 710-770 km depths (light beige).

327 The radius of curvature of a down-going slab is a useful metric to describe delam-
 328 ination because it is dependent on both the negative buoyancy of the slab and the vis-
 329 cosity ratio between the slab and upper mantle (Petersen et al., 2017; Schellart, 2010).
 330 The radius of curvature (R_c) was calculated for each delamination model every 50 model
 331 time steps. The radius of curvature calculation was adapted from the version provided
 332 in StagLab (Cramer, 2021). A least squares approximation of a circle was fit to the 1100
 333 K isotherm, which defines the core of the slab from a distance of 400 km behind the trench
 334 to a depth of 900 km. This range was chosen to include the effect of slab tip deflection
 335 resulting from the phase transitions in the mid-mantle to be used as a diagnostic tool.

336 Different stages of delamination evolution were apparent in the calculated R_c plot-
 337 ted over time (Fig. 7). The radius of curvature was largest before delamination is ini-
 338 tiated and oscillated as the plate edge began to founder. Delamination initiation is de-
 339 fined as the point when the plate edge began to bend and sink continuously, which cor-
 340 responded to the time when the radius of curvature began decreasing steadily at 2.2 Myr.
 341 The largest decrease in R_c occurred in the early stages of slab sinking as the plate be-
 342 gan bending and delaminating from the surface. The R_c in all delamination models in-
 343 creased slightly when the slab tip was deflected by postspinel density inversion at 3.8 Myr.
 344 A steady-state peel-back delamination stage was defined as the period of time from 4.0-
 345 5.9 Myr with a steadily or weakly decreasing R_c after the slab encountered the 710 km
 346 density inversions. The radius of curvature was calculated until the slab began necking
 347 prior to slab break-off at 6.5 Myr.

348 All models with the densest crust ($B_{crust} = -175 \text{ kg/m}^3$) delaminated. In order to
 349 analyze the effects of variable lithosphere thickness and maximum viscosity, R_c curves
 350 were plotted against each other (Fig. 8). Within this subset of models, all R_c evolutions
 351 contained the same major characteristic changes as model 5 described in Figure 7. The
 352 bending radius during steady-state peel-back delamination was largest for the thickest
 353 lithosphere ($h_L = 300 \text{ km}$) and decreased with decreasing plate thickness. Delamination
 354 occurred on shorter timescales for the thickest plates and initiation timescales increased
 355 with decreasing plate thickness. When lithosphere thickness was the same, the weaker
 356 plates (i.e. those with lower maximum viscosity) underwent delamination on shorter timescales
 357 than stronger plates with higher maximum viscosity.

358 3.2.2 Topography

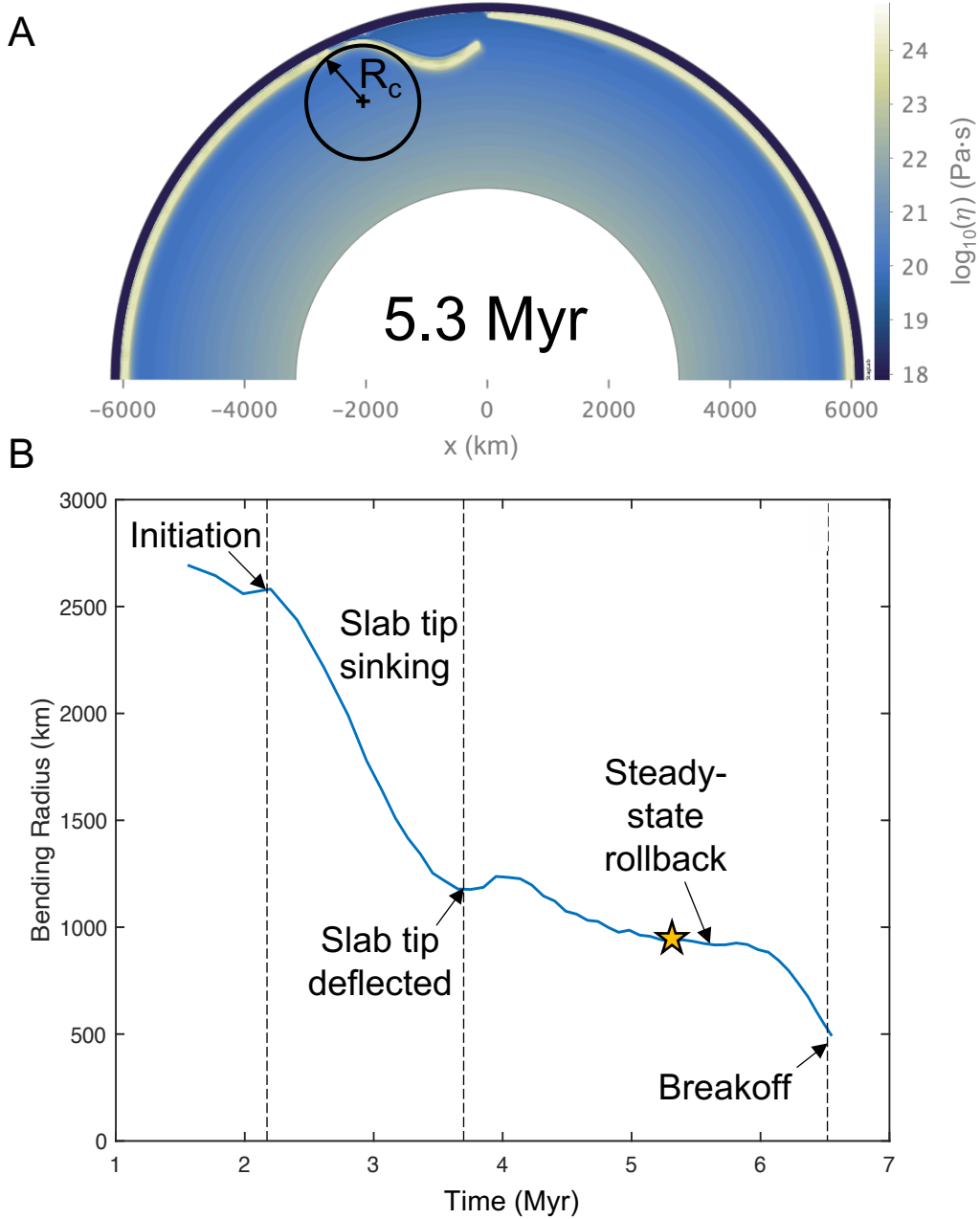


Figure 7. A least squares approximation of a circle to the 1100 K isotherm was used to estimate the radius of curvature, (R_c), during delamination. (A) The R_c for model 5 with $B_{crust} = -175 \text{ kg/m}^3$, 250 km-thick lithosphere, and $\eta_{max} = 10^{24} \text{ Pa}\cdot\text{s}$ at $t = 5.3 \text{ Myr}$ is 930.74 km (indicated by star symbol). (B) The evolution of the R_c over time for the same model. All delamination models exhibit the following features in their respective R_c evolutions: At the onset of delamination, the radius of curvature decreases sharply as the slab tip begins bending and sinking. The R_c increases briefly as the slab encounters the postspinel phase transition and then decreases slightly until reaching a relatively constant value throughout a period of steady-state peel-back delamination. The R_c decreases sharply during slab break-off.

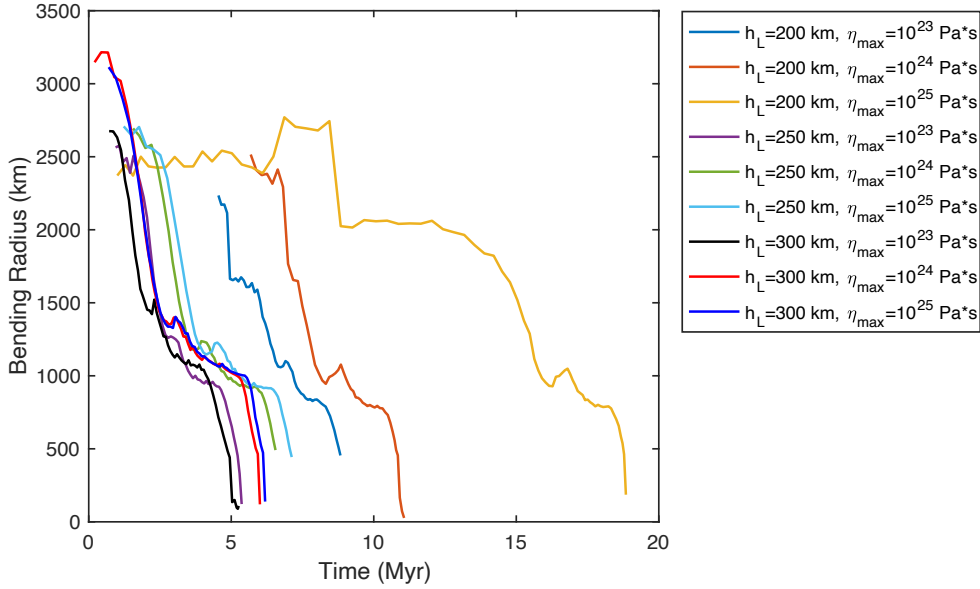


Figure 8. Radius of curvature evolution for all models with $B_{crust} = -175 \text{ kg/m}^3$, which represents the least buoyant crust. This subset of models was selected because all cases resulted in delamination. All models began at time $t=0$, but the R_c data begin when initial plate bending was detected and end prior slab break-off. Delamination occurs on faster timescales with increasing plate thickness and decreasing maximum viscosity. Maximum viscosity plays a larger role in delamination timescales when the plate is thinner and closer to neutral buoyancy.

359 Surface topography was calculated every 50 time steps for all delamination mod-
 360 els. As the plate began to delaminate, a topographic low developed at the trench near
 361 the delamination hinge, and a local topographic high was associated with the flexural
 362 bulge behind the trench of the bending plate. The height and location of the forebulge
 363 and the depth and location of the trench were tracked over time and used to estimate
 364 the timing of the end of steady-state peel-back delamination. Specific changes in trench
 365 depth, forebulge height, and their locations were identified as a precursor to slab break-
 366 off (Supplementary Fig. 2). Viscous necking at the plate hinge during slab break-off in-
 367 dicated the end of steady-state delamination.

368 *3.2.3 Delamination Timescale Analysis*

369 The timing of delamination initiation and slab break-off constrain the beginning
 370 and end of a delamination event, respectively. Initiation timing was determined using
 371 the radius of curvature and slab break-off timing was determined using the topography
 372 analyses. When all other parameters were constant, increasing positive crustal buoyancy
 373 (decreasing B_{crust}) prolonged delamination initiation and slab break-off (Fig. 9). Increas-
 374 ing plate thickness, h_L , generally caused delamination to occur on faster timescales. Weaker
 375 plates with a lower maximum viscosity delaminated on faster timescales than plates with
 376 a higher maximum viscosity. The effect of maximum viscosity on delamination initia-
 377 tion became increasingly significant for increasingly positive plate buoyancy (decreas-
 378 ing h_L and/or decreasing B_{crust}). The total duration of a delamination event also in-
 379 creased with increasing maximum plate viscosity. For example, a complete delamination
 380 event took 1.34 Myr in model 40 ($\eta_{max} = 10^{23}$ Pa·s), took 3.93 Myr in model 41 (η_{max}
 381 $= 10^{24}$ Pa·s), and took 6.77 Myr in model 42 ($\eta_{max} = 10^{25}$ Pa·s). This effect became
 382 stronger with increasing crustal buoyancy.

383 *3.2.4 Net Plate Buoyancy*

384 On Earth, subduction is driven by the negative buoyancy of oceanic plates with
 385 respect to the underlying mantle. The net buoyancy of the lithosphere can be used to
 386 determine if a plate has a propensity to sink or remain at the surface. Net plate buoy-
 387 ancy was controlled by two of the three variables in our parameter space: lithosphere thick-
 388 ness and crust density. Increasing both crust density and lithosphere thickness increases
 389 the net-negative buoyancy of the plate. The total density of each plate was calculated
 390 as a function of depth, including both thermal and compositional components (Fig. 10).

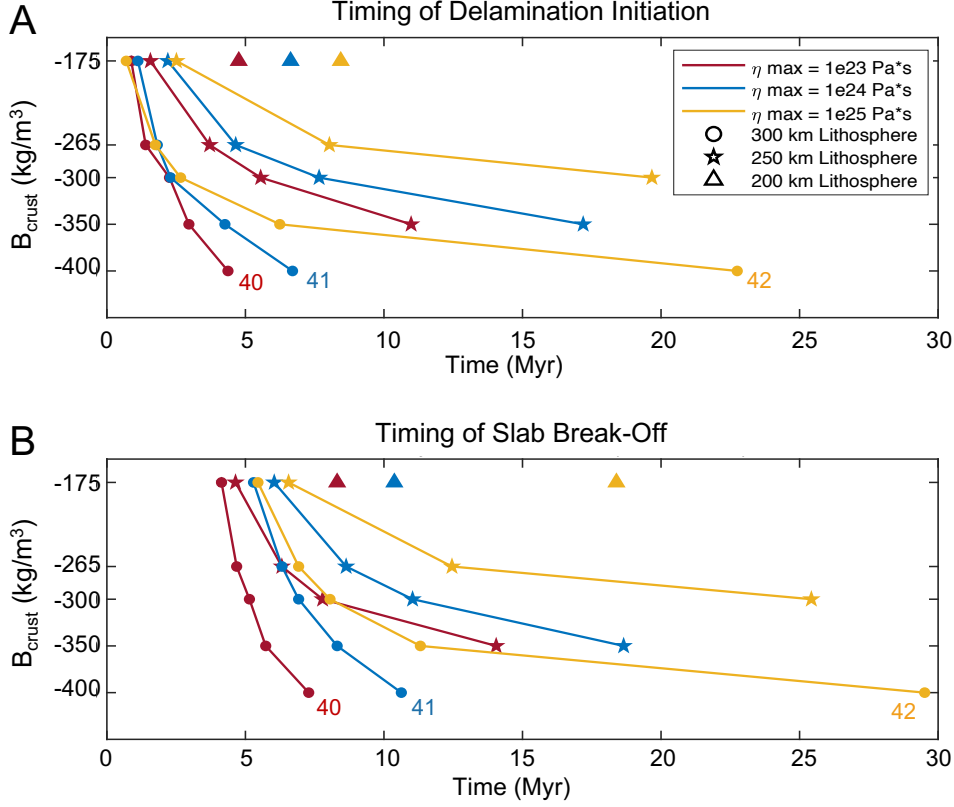


Figure 9. The timing of delamination initiation (A) and the timing of slab break-off (B) are plotted for each model that underwent peel-back delamination. Solid lines connect models with identical maximum viscosity and lithosphere thickness to highlight the effect of crustal buoyancy on delamination progression. Increasing crustal buoyancy (decreasing B_{crust}) increases the time it takes for delamination to be initiated and completed. When B_{crust} is constant, delamination occurs on faster timescales for thick, weak plates. Model numbers (see Table 2) are included for models that are discussed in this section.

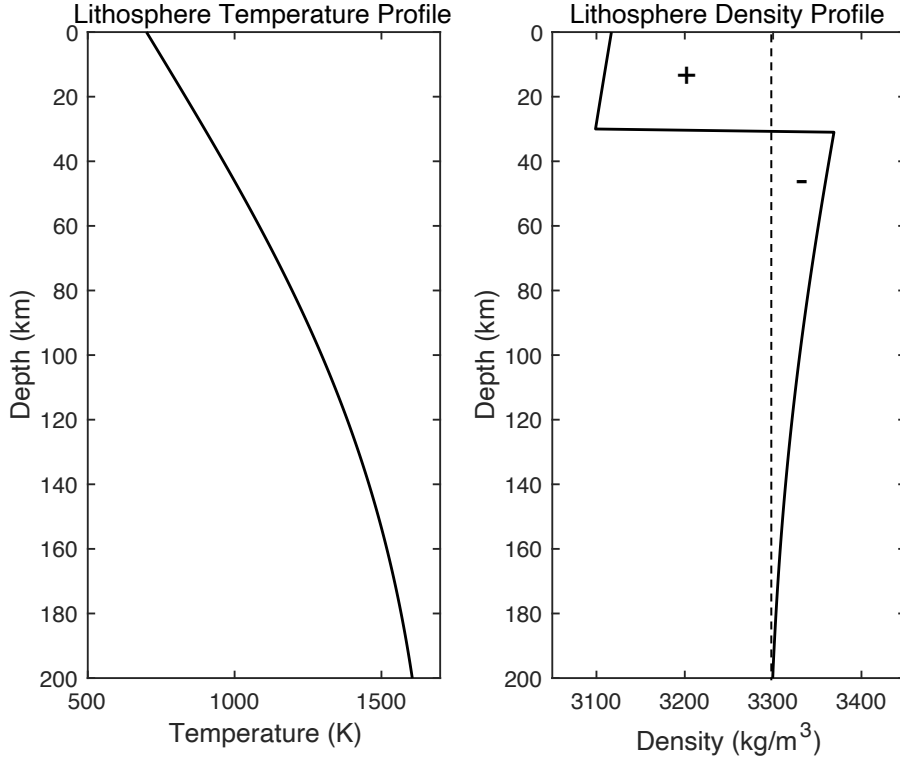


Figure 10. The temperature profile through the depth of the lithosphere (left) is used to calculate the density profile through depth (right) for each combination of lithosphere thickness and crustal buoyancy. Shown here is a 200 km-thick plate with $B_{crust} = -265 \text{ kg/m}^3$ corresponding to models 10-12. The density profile includes both compositional and thermal density contributions. The reference density of the underlying mantle, $\rho_0 = 3300 \text{ kg/m}^3$, (dotted line) differentiates positively and negatively buoyant regions within the lithosphere.

391 A density profile was calculated for each combination of lithosphere thickness and
 392 buoyancy in the model suite. The density profiles were integrated over depth to obtain
 393 a single value, $\Delta\rho_{plate}$, describing the net density contrast of the plate with respect to
 394 the underlying mantle:

$$\Delta\rho_{plate} = \int_0^{h_L} (\rho(z) - \rho_0) dz \quad (5)$$

395 The outcomes of all models are plotted in a regime diagram as a function of the
 396 net plate buoyancy and maximum viscosity (Fig. 11). All plates that were negatively
 397 buoyant with respect to the underlying mantle delaminated; however, a subset of pos-
 398 itively buoyant plates delaminated as well. This highlights a key difference between the

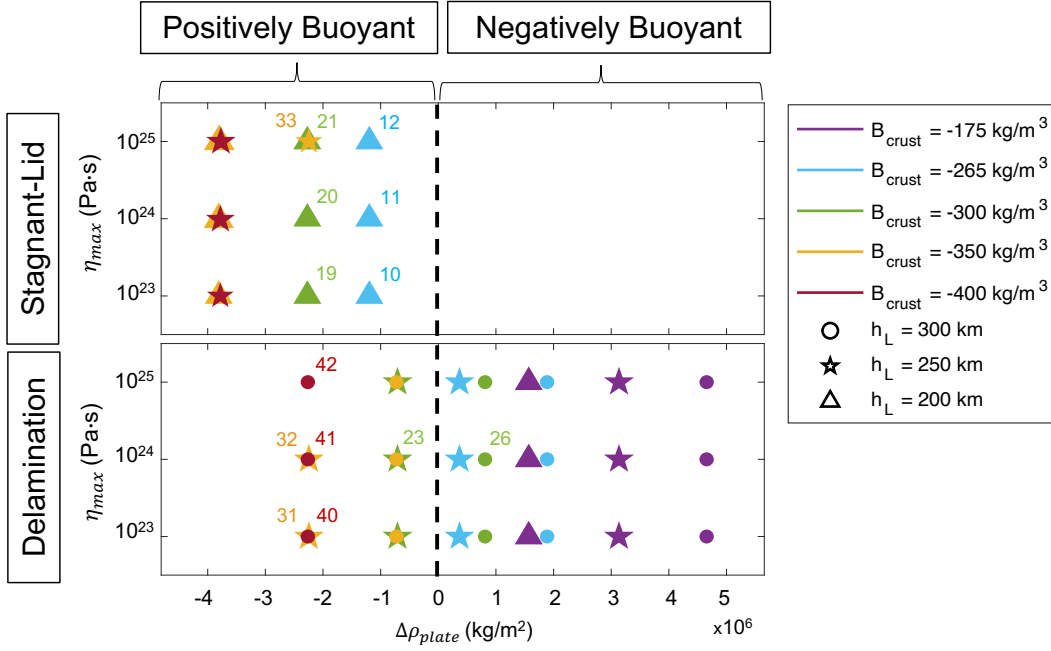


Figure 11. Tectonic regime outcomes are plotted for maximum viscosity vs integrated plate density. Stagnant-lid models (top) are separated from delamination models (bottom). Model numbers (see Table 2) are included for those mentioned in the discussion. Plates with a positive integrated density contrast ($\Delta\rho_{plate}$) with respect to the underlying mantle have a net-negative plate buoyancy, while a negative $\Delta\rho_{plate}$ corresponds to a net-positive plate buoyancy. All negatively buoyant plates delaminated. A subset of positively buoyant plates also delaminated (lower left quadrant), even though other models with nearly identical net plate buoyancy were stagnant-lid.

399 mechanisms driving subduction and delamination: negative net plate buoyancy is not
 400 required for lithospheric recycling via peel-back delamination.

401 **4 Discussion**

402 *4.1 Peel-Back Delamination Initiation*

403 To understand why certain positively buoyant plates delaminate but others with
 404 the same net buoyancy do not, we must understand the mechanisms driving peel-back
 405 delamination. Delamination is a form of lithospheric recycling in which the sub-crustal
 406 lithospheric mantle (SCLM) detaches and peels away from a layer of overlying crust re-
 407 maining at the surface. Peel-back delamination propagates along the Moho (the largest
 408 strength discontinuity over the depth of the plate) where weak, buoyant crust is juxta-
 409 posed with stronger, more negatively buoyant lithospheric mantle. Like subduction, the
 410 delamination mechanism is primarily driven by the excess density of the lithospheric man-
 411 tle with respect to the underlying asthenosphere (Bird, 1979). Thus, delamination is fa-
 412 cilitated by plates having a thick, negatively buoyant mantle lithosphere.

413 We model a compositionally-homogeneous upper mantle, so the colder lithospheric
 414 mantle is always negatively buoyant with respect to the sub-lithospheric mantle. How-
 415 ever, delamination is resisted by (1) the coupling of the plate across the lower crust-upper
 416 mantle boundary and (2) the viscous strength of the mantle. A low-viscosity lower crust
 417 layer allows mechanical decoupling along the crust-mantle boundary which is crucial for
 418 delamination to occur (Chen, 2021; Göğüş & Ueda, 2018; Krystopowicz & Currie, 2013;
 419 Magni et al., 2013; Meissner & Mooney, 1998). Early in our delamination model evo-
 420 lutions, the yield strength of the crust is exceeded near the plate edge due to extensional
 421 stresses resulting from the initial displacement of the gravitationally unstable lithospheric
 422 mantle. Consequently, the yielded crust forms a low-viscosity layer which facilitates de-
 423 coupling of the crust from the lithospheric mantle. The amount of crustal yielding in-
 424 creases by increasing the thickness of the lithosphere and therefore increasing its neg-
 425 ative buoyancy (Fig. 12). Within the subset of net-positively buoyant plates, the thick-
 426 est plates ($h_L = 300$ km) always delaminated while the thinnest plates ($h_L = 200$ km)
 427 always remained stagnant-lid. This dichotomy was even observed when the 200 and 300
 428 km-thick plates had nearly identical net plate buoyancy (Fig. 11: see models 19-21 vs.
 429 models 38-40). Even when the 200 km plate was more net-negatively buoyant than the
 430 300 km plate, it still remained stable in the stagnant lid regime (Fig. 11: see models 10-

431 12 vs models 38-40). The thinner lithosphere to the right of the gap ($h_{L-min} = 100$ km)
 432 never delaminated because there is less negative buoyancy to overcome the coupling of
 433 the crust and lithosphere. When the lithospheric mantle portion of the plate is sufficiently
 434 dense, the forces driving delamination prevail; however when the lithospheric mantle has
 435 insufficient negative buoyancy, plate coupling inhibits delamination.

436 It is worth reiterating that delamination is driven by the negative buoyancy of the
 437 lithospheric mantle with respect to the underlying mantle, and not the density contrast
 438 across the Moho. While it may seem reasonable to assume that increasing the den-
 439 sity contrast between the crust and lithosphere would always promote decoupling, vary-
 440 ing crustal buoyancy has a more complicated effect. This can be observed in the sub-
 441 set of positively buoyant plates with a 250 km-thick lithosphere: those closer to neutral
 442 buoyancy delaminated ($B_{crust} = [-300, -350]$ kg/m³), while increasing crustal buoyancy
 443 favored a stagnant-lid outcome ($B_{crust} = [-350, -400]$ kg/m³) (Fig. 11). Although the
 444 lithospheric mantle portion of the plate maintained the same integrated negative buoy-
 445 ancy, increasing the positive buoyancy of the crust (and therefore the entire plate) in-
 446 hibits delamination. The positive buoyancy of the crust resists plate bending, thereby
 447 preventing crustal yielding and the development of the weak zone required for delam-
 448 ination. Compared to thicker plates with excess negative buoyancy, thinner plates re-
 449 quire less positively buoyant crust in order to undergo bending and delamination.

450 *4.2 Plate Strength*

451 In addition to plate coupling across the crust-mantle boundary, the viscous strength
 452 of the lithospheric mantle is another resisting force to delamination. By varying the max-
 453 imum viscosity of our models over two orders of magnitude [10^{23} , 10^{24} , 10^{25} Pa·s], we
 454 systematically varied the strength of the cold upper portion of the lithosphere. The en-
 455 ergy required for plate bending is proportional to its viscosity; therefore plate bending,
 456 which is required for the formation of the delamination weak zone, becomes more dif-
 457 ficult with increasing maximum viscosity. For example, models 32 and 33 were identi-
 458 cal except for a one order-of-magnitude difference in maximum viscosity ($\eta_{max,32} = 10^{24}$
 459 Pa·s and $\eta_{max,33} = 10^{25}$ Pa·s). The weaker plate in model 32 delaminated while the stronger
 460 plate in model 33 remained a stagnant lid (Fig. 13). The effect of increasing maximum
 461 viscosity can further be observed in the timescales of delamination (Fig. 9). In models
 462 with identical lithosphere thickness and crustal buoyancy, increasing maximum viscos-

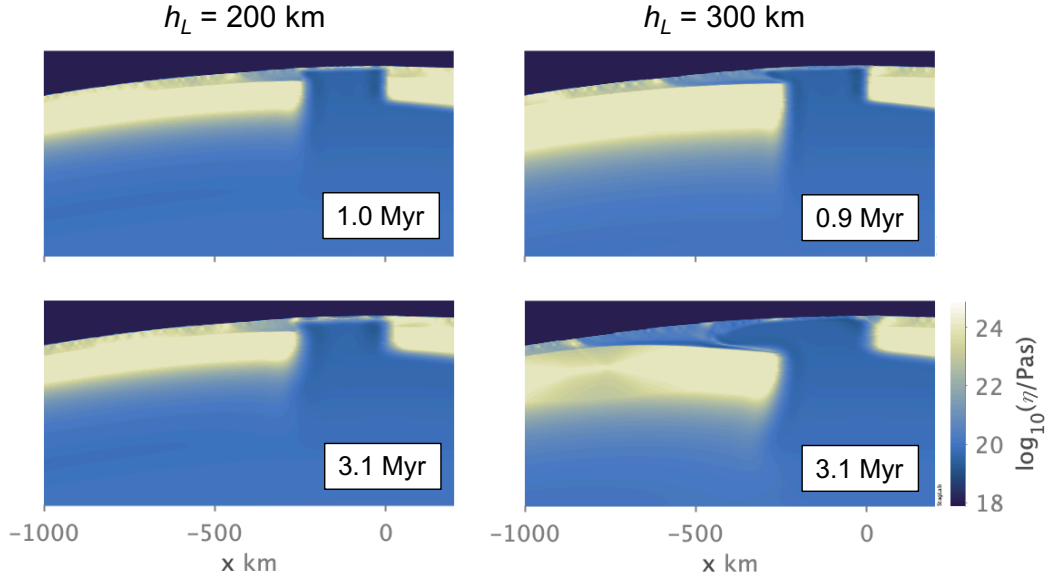


Figure 12. Viscosity field comparison of crust yielding and weak zone formation for stagnant-lid model 20 (left) vs. delamination model 26 (right). Models were identical ($B_{crust} = -300$ kg/m³, $\eta_{max} = 10^{24}$ Pa·s) except for plate thickness. The 300 km-thick plate in model 26 has a thicker and denser lithospheric mantle, causing it to bend further and induce more crustal yielding over the plate edge. The yielded crust is weak and facilitates decoupling and delamination of the lithospheric mantle. Although some crust weakening is observed over the plate edge of model 20, its thinner lithospheric mantle has less negative buoyancy to form a sufficient delamination weak zone. If the crust is yielded but delamination is not initiated (left), the strength (i.e. viscosity) of the weakened crust increases over time.

463 ity increases the timescales of the delamination process. The effect of maximum viscos-
 464 ity on delamination timing becomes increasingly important with increasing crustal buoy-
 465 ancy, because increasing crustal buoyancy also prolongs delamination. When the crust
 466 is more positively buoyant, it takes significantly longer for the strongest plate (e.g. model
 467 42) to go unstable than the weakest plate (e.g. model 40) due to the combination of ef-
 468 fects which discourage plate bending.

469 The viscous strength of the mantle as a resisting force to delamination not only refers
 470 to the strength of the plate itself, but also the resistance of the sublithospheric mantle
 471 to deformation from a sinking plate. Although we did not vary the radial viscosity over
 472 the depth of the mantle, a higher viscosity asthenosphere would inhibit delamination and

473 prolong timescales of delamination, while a weak asthenosphere may promote delami-
 474 nation on shorter timescales. We used a single value for mantle potential temperature
 475 (1700 K), but we expect that higher temperatures would favor delamination on shorter
 476 timescales. A warmer interior would decrease the viscosity of the sublithospheric man-
 477 tle, which would facilitate delamination. Warmer mantle temperatures and higher tem-
 478 perature gradients across the lithosphere would reduce plate strength, which would also
 479 facilitate plate bending and delamination. Conversely, a colder mantle temperature would
 480 likely inhibit delamination and slab sinking. Such details can be pursued by future in-
 481 vestigations.

482 *4.3 Crustal Thickness and Buoyancy*

483 Gravity and topography predict large regional variations in Venus' crustal thick-
 484 ness (0-110 km) (Anderson & Smrekar, 2006) and estimates for the average crustal thick-
 485 ness typically fall between 8-50 km (James et al., 2013). Variations in crustal thickness
 486 may have a complicated effect on delamination initiation. On one hand, thicker layers
 487 of buoyant crust will increase the positive buoyancy of the plate and inhibit plate bend-
 488 ing and delamination. However, increasing crustal thickness in our models would result
 489 in less cold, strong lithospheric mantle to resist plate bending. The basalt-eclogite tran-
 490 sition occurs at deeper depths in Venus' mantle than on Earth, requiring crust to subduct
 491 to deeper depths before the added negative buoyancy from eclogite can help sustain de-
 492 lamination. Yet if crust on Venus is thicker than on Earth, less crust displacement is nec-
 493 essary for eclogitization depths to be reached. If we consider a multi-stage basalt-eclogite
 494 transition beginning at shallower depths than 70 km (Ito & Kennedy, 1971), a thick layer
 495 of crust may reduce the compositional buoyancy of the crust and stimulate recycling of
 496 the lower crust and lithosphere on faster timescales.

497 Not all models of global episodic overturns consider the chemical buoyancy of the
 498 crust and its effect on subduction (Weller & Kiefer, 2020), and others may underestimate
 499 its effect (Armann & Tackley, 2012; Crameri & Tackley, 2016; Rolf et al., 2018; Uppala-
 500 pati et al., 2020). To isolate the effect of crustal buoyancy on lithospheric recycling, we
 501 varied the density contrast of the crust, B_{crust} , over 5 values (-175 to -400 kg/m³) for
 502 a uniformly-thick crust ($h_{crust} = 30$ km). Our results indicate that the chemical buoy-
 503 ancancy of the crust is an important factor understanding delamination initiation because
 504 it (1) affects the net buoyancy of the plate and (2) resists the bending of the lithospheric

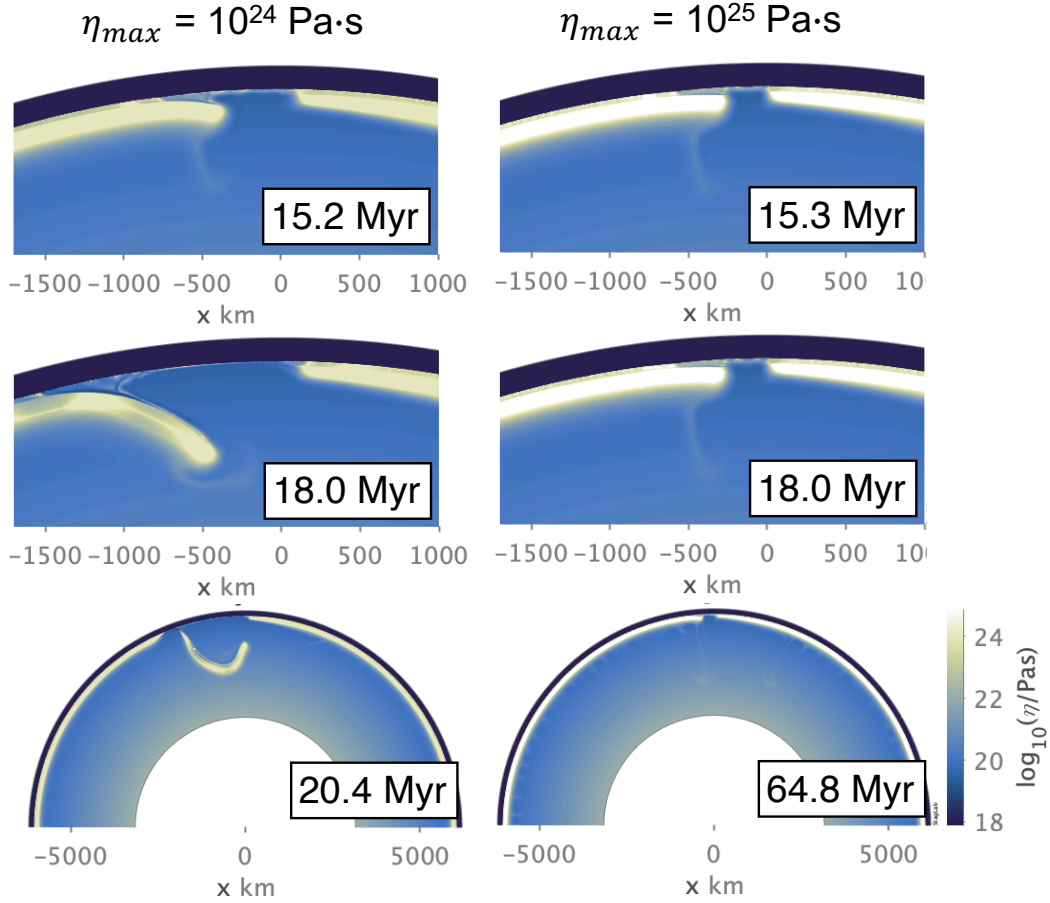


Figure 13. Viscosity field comparison of model 31 with a maximum viscosity of 10^{24} Pa·s (left) vs. model 32 with a maximum viscosity of 10^{25} Pa·s (right). Both plates are positively buoyant with identical net buoyancy, plate thickness ($h_L = 250$ km) and crust buoyancy ($B_{crust} = -350$ kg/m³). The weaker plate is able to undergo bending and delamination, yet only a one order-of-magnitude increase in viscosity causes the stronger plate to resist bending and remain immobile.

505 mantle that is a precursor to delamination. More work will need to be done to under-
 506 stand the role that crustal thickness and buoyancy play on the different styles of resur-
 507 facing proposed for Venus.

508 4.4 Yield Stress

509 For Earth, there is a discrepancy between the maximum yield stress predicted by
 510 laboratory experiments (Kohlstedt et al., 1995) and those used in numerical models to
 511 study subduction (Tackley, 2008). A mobile-lid is generally favored when the yield strength

512 parameterization is limited by a low maximum yield stress with depth, and increasing
 513 the maximum yield stress promotes a stagnant-lid (Moresi & Solomatov, 1998). Armann
 514 and Tackley (2012) found that 5-8 global overturns can occur when the yield stress is
 515 limited to 100 MPa (Armann & Tackley, 2012) and other studies have modeled global
 516 overturns on Venus by employing similarly low yield stresses (Crameri & Tackley, 2016;
 517 Rolf et al., 2018; Weller & Kiefer, 2020; Uppalapati et al., 2020). Higher yield stresses
 518 (up to 300 MPa) also produced global overturns, though the duration of the mobile-lid
 519 period was shorter and less vigorous (Armann & Tackley, 2012).

520 Since the yield strength profile with depth is even less constrained for Venus, we
 521 tested a higher limiting yield stress (500 MPa) than in previous global overturn mod-
 522 els. We were able to model regional-scale lithospheric resurfacing with a relatively high
 523 yield stress in part because the the crust strength is limited by a relatively low yield stress
 524 (surface cohesion = 10 MPa). Venus' lower crust is predicted by some to be weak rel-
 525 ative to the upper crust and underlying lithospheric mantle and deformable on relatively
 526 short geologic timescales (Arkani-Hamed, 1993; Azuma et al., 2014; Buck, 1992; Ghail,
 527 2015; Katayama, 2021; Zuber, 1987). Previous experimental studies may have overes-
 528 timated the strength of Venus' crust (Mackwell et al., 1998) by using diabase instead of
 529 plagioclase at the brittle-ductile transition where Peierls creep is the primary deforma-
 530 tion mechanism (Azuma et al., 2014; Katayama, 2021). We also consider that crustal
 531 yielding and weak zone formation is driven by extensional forces in the crust owing to
 532 the gravitational instability of the lithospheric mantle. In this context, a weak crust pa-
 533 rameterization may be appropriate since the yield strength of the crust is expected to
 534 be lower under extension than compression. A higher crustal yield strength would in-
 535 hibit weak zone formation; delamination would likely require thicker lithospheres in or-
 536 der to generate sufficient stresses in the crust.

537 Still, the weak zone could come from a variety of tectonic processes, including melt-
 538 ing and thermal weakening near the Moho (Faccenda et al., 2009; Ueda et al., 2012) and
 539 intrusive magmatism in the lithosphere (Lourenço et al., 2020). If there was a pre-existing
 540 weak zone in the plate that did not require crustal yielding, it is possible that thinner
 541 plates may also undergo delamination. Higher strength crust may still yield and form
 542 a weak zone in the presence higher lithospheric stresses due to ongoing tectonic defor-
 543 mation. The origin of the weak zone is not considered to be within the scope of this study
 544 but is important in understanding how delamination could operate on Venus.

545 *4.5 Uncertainties*

546 In our simplified rift zone setup, we model a sharp temperature gradient across a
 547 vertical boundary separating the plate edge and the gap containing relatively warm man-
 548 tle material. The lithospheric gap itself is only a first order representation for the ther-
 549 mal structure at rift zones on Venus and lacks finer details. However, it is an appropri-
 550 ate starting point as we acquire a better understanding of the relationship between the
 551 strength and buoyancy of a plate and its tendency to delaminate.

552 In the early stages of delamination, only a thin layer of crust is attached to the down-
 553 going plate. Once the crustal root reaches the eclogite transition depth, thicker layers
 554 of crust remain attached to the delaminating plate due to the eclogite density inversion
 555 (see Fig. 6). The thickness of the crustal root over the delamination hinge is important
 556 in determining how much crust is eclogitized, which has implications for slab sinking dy-
 557 namics. We imposed a minimum crust thickness of 15 km to prevent sticky-air particles
 558 from becoming embedded in the mantle material exposed at the surface of the gap due
 559 to its low viscosity contrast. Though this feature may potentially overestimate the amount
 560 of crust at the surface, we expect that new crust would be generated in the delamina-
 561 tion zone. Since our models currently do not include melting processes, the volume of
 562 crust at the surface is an approximation.

563 *4.5 Implications for Resurfacing*

564 A peel-back delamination event on Venus would undoubtedly have a unique sur-
 565 face expression. During the initial stages of delamination, it is clear that the majority
 566 of the crust remains at the surface or within the crustal root formed at the slab hinge
 567 (Fig. 4D). As the lithospheric mantle peels away, it is replaced by warm asthenosphere
 568 flowing beneath a thinned layer of crust at the surface. Delamination of the lithospheric
 569 mantle in Earth-like conditions is predicted to lead to enhanced surface magmatism, lo-
 570 cal tectonic uplift, and horizontal surface deformation in the region overlying the delam-
 571 ination zone (Bird, 1979; Göğüş & Psyklywec, 2008b; Kay & Kay, 1993). Yet, due to un-
 572 certainties in the exact volume of remaining surface crust, the style and extent of resur-
 573 facing that may follow a delamination event still remains unclear. Perhaps the delam-
 574 ination zone would be fully resurfaced due to a high degree of induced surface volcan-
 575 ism - or perhaps delamination may only be a source of surface deformation and crater

576 modification via localized, thin lava flows consistent with the regional equilibrium resur-
577 facing model (O’Rourke et al., 2014).

578 Without modeling melt processes, the extent of resurfacing will remain unclear. How-
579 ever, we can compare our results to delamination models in an Archean Earth environ-
580 ment (Chowdhury et al., 2017, 2020; Perchuk et al., 2018) when the mantle was thought
581 to be hotter (Herzberg et al., 2010) and more comparable to Venus than at present. Our
582 initial condition resembles the starting point for the initiation of “peel back convergence”
583 in a numerical modeling study of delamination in the Archean Earth by Chowdhury et
584 al. (2020) (see their Fig. 1c). Peel back convergence is described as a form of rollback
585 delamination initiated at a sharp lateral lithospheric discontinuity at a convergent mar-
586 gin (Chowdhury et al., 2020). While the weak zone delamination surface in our models
587 originated from yielding of a weak lower crust, the weak zone in Chowdhury et al. (2020)
588 was generated by melting and weakening of a protocontinental crust. Following a delam-
589 ination event, they observed a region of thinned, hot crust at the surface characterized
590 by localized volcanism, including underplating melt and rising melt domes. A more mod-
591 ern analogue on Earth may be found in East Anatolia over the Arabia-Eurasia collision
592 zone. The lithosphere beneath the East Anatolian plateau is thought to have been re-
593 cycled in an event comparable to peel-back delamination and was accompanied by sur-
594 face uplift, distinct zones of extension and compression, high heat flow, and volcanism
595 (Göğüş & Psyklywec, 2008a; Keskin, 2003; Memiş et al., 2020). Evidence for similar de-
596 lamination processes may also be present in the Southeast Carpathians (Fillerup et al.,
597 2010; Şengül Uluocak et al., 2019), the Northern Tibetan plateau (Li et al., 2016), and
598 other locations on Earth (see Memiş et al., (2020) and references therein).

599 In addition to the surface expression of a delamination event, is also important to
600 constrain the total delamination area in order to understand the extent of resurfacing
601 that is possible. The timing of slab break-off appears to be strongly influenced by the
602 slab’s interaction with the two sources of positive buoyancy near 710-770 km depth. Dur-
603 ing the steady-state delamination stage, the zone of positive buoyancy effectively helps
604 support the weight of the slab as peel-back delamination progresses at the surface. Even-
605 tually the slab sinks through this barrier, and the slab pull force (and therefore stresses
606 at the delaminating plate hinge) sharply increases, which results in yielding and neck-
607 ing of the plate at the surface in a process that is consistent between all delamination
608 models. If there was less positive buoyancy in the slab at 710 km-depth (e.g. if the Clapey-

ron slope of the postspinel transition was closer to zero), the location and timing of slab-breakoff may vary more significantly between different delamination models. Slab break-off is also influenced by the yield strength parameterization throughout the slab; if the limiting yield stress was lower, break-off may occur earlier in the delamination process as stresses accumulate in the slab hinge. We estimate the total length of a single peel-back delamination event to be between 2500-3000 km (approximately 1/7 of the surface). Since our models are two dimensional, we possibly over- or underestimate the scale of the delamination zone. Future directions may include modeling peel-back delamination in 3D, since three-dimensional models are important for understanding the mantle dynamics and tectonics associated with the toroidal component of flow induced by a sinking slab (Stegman et al., 2006; Schellart et al., 2007). This may have implications for slab sinking geometry, predicted melt volumes, and total amount of resurfacing that may occur during a delamination event.

5 Conclusions

Despite the thousands of kilometers of chasma rift zones that have been identified as potential subduction sites on Venus (Sandwell & Schubert, 1992; Schubert & Sandwell, 1995), there have been no studies to date which have investigated the dynamics of lithospheric recycling initiated at Venusian rift zones. Here, we presented the first 2D numerical models to indicate that peel-back delamination initiated at a lateral lithospheric discontinuity may be a viable mechanism for lithospheric recycling and heat loss on Venus. Delamination has been proposed to occur on Venus, however it is typically studied within the context of plume-lithosphere interactions and coronae formation (Ashwal et al., 1988; Davaille et al., 2017; Gülcher et al., 2020; Smrekar & Stofan, 1997). We showed that in the absence of plume-lithosphere interactions, the full depth of the sub-crustal lithospheric mantle can detach and peel away from the crust remaining at the surface.

Delamination is primarily driven by the excess density of the lithospheric mantle. It requires a weak lower crust for decoupling to propagate and a connection between the Moho and asthenosphere for buoyant material to rise and fill the space between the crust and down-going plate. When these criteria are satisfied we observe that, unlike subduction, both net-positively and net-negatively buoyant plates may undergo delamination. Our results indicate that positive crustal buoyancy inhibits delamination by impeding plate bending which drives crust yielding and weak zone formation. However once the

641 crust reaches the basalt-eclogite transition depth, the eclogite density inversion helps sus-
642 tain delamination. Delamination may only occur when the mantle lithosphere is suffi-
643 ciently negatively buoyant to bend and counteract the initial positive buoyancy of the
644 crust. In cases with insufficient mantle lithosphere thickness, excess crustal buoyancy,
645 or the absence of a conduit connecting crust and asthenosphere, a stagnant-lid regime
646 may persist.

647 Peel-back delamination may have important implications as a source of regional-
648 scale resurfacing within the framework of the regional equilibrium resurfacing (RER) hy-
649 pothesis. Following a delamination event, the emplacement of hot asthenosphere beneath
650 a layer of thinned crust may enhance surface deformation and volcanism. Perhaps the
651 evidence for the highly deformed (Byrne et al., 2020) and globally fragmented lithosphere
652 (Byrne et al., 2021) can be viewed as forms of surface tectonics associated with delam-
653 ination events. Not only is delamination compatible with Venus’ style of surface defor-
654 mation, but it may be responsible for some of the observed heterogeneity in crust and
655 lithosphere thickness (Anderson & Smrekar, 2006). Though more work will need to be
656 done to determine if it can satisfy cratering and CM-CF offset constraints, the regional-
657 scale peel-back delamination regime may be able to explain some aspects of Venus’ unique
658 resurfacing history.

659 **Acknowledgments**

660 Authors are grateful for support from NASA Award 80NSSC22K0100. Computa-
661 tional resources were provided by Extreme Science and Engineering Discovery Environ-
662 ment (XSEDE), which is supported by National Science Foundation grant number ACI-
663 1053575. The authors are grateful for technical assistance from Fabio Cramer, acknowl-
664 edge helpful reviews from two anonymous referees, and thank David Sandwell for help-
665 ful discussions. A. Adams also thanks CIG for travel support to 2019 Ada Lovelace Work-
666 shop on Modelling Mantle and Lithosphere Dynamics.

667 **6 Open Research**

668 The model data from this study are available in an online repository (Adams, 2022).
669 StagYY is the property of P.J.T., and is available upon request for collaborative stud-
670 ies. Requests can be made to P.J.T. (paul.tackley@erdw.ethz.ch).

671 **References**

- 672 Adams, A. C. (2022). *Regional-scale lithospheric recycling on venus via peel-back*
 673 *delamination*. Zenodo. Retrieved from [https://doi.org/10.5281/zenodo](https://doi.org/10.5281/zenodo.6819751)
 674 [.6819751](https://doi.org/10.5281/zenodo.6819751) doi: 10.5281/zenodo.6819751
- 675 Akaogi, M., & Ito, E. (1993). Refinement of enthalpy measurement of mgsio 3 per-
 676 ovskite and negative pressure-temperature slopes for perovskite-forming reac-
 677 tions. *Geophysical Research Letters*, *20*, 1839-1842. doi: 10.1029/93GL01265
- 678 Anderson, F. S., & Smrekar, S. E. (2006). Global mapping of crustal and litho-
 679 spheric thickness on venus. *Journal of Geophysical Research E: Planets*, *111*.
 680 doi: 10.1029/2004JE002395
- 681 Arkani-Hamed, J. (1993). On the tectonics of venus. *Physics of the Earth and Plan-*
 682 *etary Interiors*, *76*, 75-96. doi: 10.1016/0031-9201(93)90056-F
- 683 Armann, M., & Tackley, P. J. (2012). Simulating the thermochemical magmatic and
 684 tectonic evolution of venus's mantle and lithosphere: Two-dimensional models.
 685 *Journal of Geophysical Research: Planets*, *117*. doi: 10.1029/2012JE004231
- 686 Ashwal, L. D., Burke, K., & Sharpton, V. L. (1988). Lithospheric delamination
 687 on earth and venus. *Abstracts of the Lunar and Planetary Science Conference*,
 688 *19*, 17.
- 689 Azuma, S., Katayama, I., & Nakakuki, T. (2014). Rheological decoupling at the
 690 moho and implication to venusian tectonics. *Scientific Reports*, *4*, 1-5. doi: 10
 691 [.1038/srep04403](https://doi.org/10.1038/srep04403)
- 692 Basilevsky, A. T., & Head, J. W. (2002). Venus: Timing and rates of geologic activ-
 693 ity. *Geology*, *30*, 1015. doi: 10.1130/0091-7613(2002)030<1015:VTAROG>2.0
 694 [.CO;2](https://doi.org/10.1130/0091-7613(2002)030<1015:VTAROG>2.0.CO;2)
- 695 Bird, P. (1979). Continental delamination and the colorado plateau. *Journal of Geo-*
 696 *physical Research*, *84*. doi: 10.1029/JB084iB13p07561
- 697 Bjornes, E. E., Hansen, V. L., James, B., & Swenson, J. B. (2012). Equi-
 698 librium resurfacing of venus: Results from new monte carlo modeling
 699 and implications for venus surface histories. *Icarus*, *217*, 451-461. doi:
 700 [10.1016/j.icarus.2011.03.033](https://doi.org/10.1016/j.icarus.2011.03.033)
- 701 Buck, W. R. (1992). Global decoupling of crust and mantle: Implications for to-
 702 pography, geoid and mantle viscosity on venus. *Geophysical Research Letters*,
 703 *9*, 2111-2114. doi: 10.1029/92GL02462

- 704 Bullock, M. A., Grinspoon, D. H., & Head, J. W. (1993). Venus resurfacing rates:
 705 Constraints provided by 3-d monte carlo simulations. *Geophysical Research*
 706 *Letters*, *20*, 2147-2150. doi: 10.1029/93GL02505
- 707 Byrne, P. K., Ghail, R. C., Gilmore, M. S., Şengör, A. M., Klimczak, C., Senske,
 708 D. A., ... Solomon, S. C. (2020, 1). Venus tesserae feature layered, folded, and
 709 eroded rocks. *Geology*, *49*, 81-85. doi: 10.1130/G47940.1
- 710 Byrne, P. K., Ghail, R. C., Şengör, A. M., James, P. B., Klimczak, C., &
 711 Solomon, S. C. (2021). A globally fragmented and mobile lithosphere
 712 on venus. *Proceedings of the National Academy of Sciences*, *118*. doi:
 713 10.1073/pnas.2025919118
- 714 Chen, L. (2021). The role of lower crustal rheology in lithospheric delamination dur-
 715 ing orogeny. *Frontiers in Earth Science*, *9*. doi: 10.3389/feart.2021.755519
- 716 Chowdhury, P., Chakraborty, S., Gerya, T. V., Cawood, P. A., & Capitanio, F. A.
 717 (2020). Peel-back controlled lithospheric convergence explains the secular
 718 transitions in archean metamorphism and magmatism. *Earth and Planetary*
 719 *Science Letters*, *538*. doi: 10.1016/j.epsl.2020.116224
- 720 Chowdhury, P., Gerya, T., & Chakraborty, S. (2017). Emergence of silicic continents
 721 as the lower crust peels off on a hot plate-tectonic earth. *Nature Geoscience*,
 722 *10*, 698-703. doi: 10.1038/ngeo3010
- 723 Crameri, F. (2021). *Staglab*. Zenodo. Retrieved from [https://doi.org/10.5281/](https://doi.org/10.5281/zenodo.5005427)
 724 [zenodo.5005427](https://doi.org/10.5281/zenodo.5005427) doi: 10.5281/zenodo.5005427
- 725 Crameri, F., Lithgow-Bertelloni, C. R., & Tackley, P. J. (2017). The dynamical
 726 control of subduction parameters on surface topography. *Geochemistry, Geo-*
 727 *physics, Geosystems*, *18*, 1661-1687. doi: 10.1002/2017GC006821
- 728 Crameri, F., Schmeling, H., Golabek, G. J., Duretz, T., Orendt, R., Buitert,
 729 S. J. H., ... Tackley, P. J. (2012). A comparison of numerical surface
 730 topography calculations in geodynamic modelling: an evaluation of the
 731 'sticky air' method. *Geophysical Journal International*, *189*, 38-54. doi:
 732 10.1111/j.1365-246X.2012.05388.x
- 733 Crameri, F., & Tackley, P. J. (2016). Subduction initiation from a stagnant lid
 734 and global overturn: new insights from numerical models with a free surface.
 735 *Progress in Earth and Planetary Science*, *3*. doi: 10.1186/s40645-016-0103-8
- 736 Davaille, A., Smrekar, S. E., & Tomlinson, S. (2017). Experimental and observa-

- 737 tional evidence for plume-induced subduction on venus. *Nature Geoscience*,
738 *10*, 349-355. doi: 10.1038/ngeo2928
- 739 Davies, G. F. (2008). Episodic layering of the early mantle by the 'basalt barrier'
740 mechanism. *Earth and Planetary Science Letters*, *275*, 382-392. doi: 10.1016/
741 j.epsl.2008.08.036
- 742 Elkins-Tanton, L. T. (2007). Continental magmatism, volatile recycling, and a het-
743 erogeneous mantle caused by lithospheric gravitational instabilities. *Journal of*
744 *Geophysical Research: Solid Earth*, *112*. doi: 10.1029/2005JB004072
- 745 Faccenda, M., Minelli, G., & Gerya, T. V. (2009). Coupled and decoupled regimes
746 of continental collision: Numerical modeling. *Earth and Planetary Science Let-*
747 *ters*, *278*, 337-349. doi: 10.1016/j.epsl.2008.12.021
- 748 Fei, Y., Orman, J. V., Li, J., van Westrenen, W., Sanloup, C., Minarik, W., ... Fu-
749 nakoshi, K. (2004). Experimentally determined postspinel transformation
750 boundary in mg₂sio₄ using mgo as an internal pressure standard and its geo-
751 physical implications. *Journal of Geophysical Research: Solid Earth*, *109*. doi:
752 10.1029/2003jb002562
- 753 Feuvre, M. L., & Wiczorek, M. A. (2011). Nonuniform cratering of the moon and a
754 revised crater chronology of the inner solar system. *Icarus*, *214*, 1-20. doi: 10
755 .1016/j.icarus.2011.03.010
- 756 Fillerup, M. A., Knapp, J. H., Knapp, C. C., & Raileanu, V. (2010). Mantle earth-
757 quakes in the absence of subduction? continental delamination in the roma-
758 nian carpathians. *Lithosphere*, *2*, 333-340. doi: 10.1130/L102.1
- 759 Fukao, Y., Obayashi, M., Nakakuki, T., Utada, H., Suetsugu, D., Irifune, T., ...
760 Hirose, K. (2009). Stagnant slab: A review. *Annual Review of Earth and*
761 *Planetary Sciences*, *37*, 19-46. doi: 10.1146/annurev.earth.36.031207.124224
- 762 Ghail, R. (2015). Rheological and petrological implications for a stagnant lid regime
763 on venus. *Planetary and Space Science*, *113-114*, 2-9. doi: 10.1016/j.pss.2015
764 .02.005
- 765 Gögüş, O. H., & Ueda, K. (2018). Peeling back the lithosphere: Controlling param-
766 eters, surface expressions and the future directions in delamination modeling.
767 *Journal of Geodynamics*, *117*, 21-40. doi: 10.1016/j.jog.2018.03.003
- 768 Gögüş, O. H., & Psyklywec, R. N. (2008a). Mantle lithosphere delamination driving
769 plateau uplift and synconvergent extension in eastern anatolia. *Geology*, *36*,

- 770 723-726. doi: 10.1130/G24982A.1
- 771 Göğüş, O. H., & Psyklywec, R. N. (2008b). Near-surface diagnostics of dripping or
772 delaminating lithosphere. *Journal of Geophysical Research: Solid Earth*, *113*.
773 doi: 10.1029/2007JB005123
- 774 Göğüş, O. H., Psyklywec, R. N., Şengör, A. M., & Gün, E. (2017). Drip tectonics
775 and the enigmatic uplift of the central anatolian plateau. *Nature Communica-*
776 *tions*, *8*. doi: 10.1038/s41467-017-01611-3
- 777 Gülcher, A. J., Gerya, T. V., Montési, L. G., & Munch, J. (2020). Corona
778 structures driven by plume–lithosphere interactions and evidence for on-
779 going plume activity on venus. *Nature Geoscience*, *13*, 547-554. doi:
780 10.1038/s41561-020-0606-1
- 781 Hansen, V. L., & Young, D. A. (2007). Venus’s evolution: A synthesis. *Special*
782 *Paper of the Geological Society of America*, *419*, 255-273. doi: 10.1130/2006
783 .2419(13)
- 784 Hernlund, J. W., & Tackley, P. J. (2008). Modeling mantle convection in the spher-
785 ical annulus. *Physics of the Earth and Planetary Interiors*, *171*, 48-54. doi: 10
786 .1016/j.pepi.2008.07.037
- 787 Herrick, R. R. (1994). Resurfacing history of venus. *Geology*, *22*, 703-706. doi: 10
788 .1130/0091-7613(1994)022<0703:RHOV>2.3.CO;2
- 789 Herrick, R. R., & Rumpf, M. E. (2011). Postimpact modification by volcanic or tec-
790 tonic processes as the rule, not the exception, for venusian craters. *Journal of*
791 *Geophysical Research E: Planets*, *116*. doi: 10.1029/2010JE003722
- 792 Herzberg, C., Condie, K., & Korenaga, J. (2010). Thermal history of the earth
793 and its petrological expression. *Earth and Planetary Science Letters*, *292*, 79-
794 88. doi: 10.1016/j.epsl.2010.01.022
- 795 Houseman, G. A., & Molnar, P. (1997). Gravitational (rayleigh-taylor) insta-
796 bility of a layer with non-linear viscosity and convective thinning of conti-
797 nental lithosphere. *Geophysical Journal International*, *128*, 125-150. doi:
798 10.1111/j.1365-246X.1997.tb04075.x
- 799 Irifune, T., Nishiyama, N., Kuroda, K., Inoue, T., Isshiki, M., Utsumi, W.,
800 ... Ohtaka, O. (1998). The postspinel phase boundary in mg₂siO₄ de-
801 termined by in situ x-ray diffraction. *Science*, *279*, 1698-1700. doi:
802 10.1126/science.279.5357.1698

- 803 Ito, K., & Kennedy, G. C. (1971). An experimental study of the basalt-garnet
804 granulite-eclogite transition. *Geophysical Monography Series*, *14*, 303-314. doi:
805 10.1029/GM014p0303
- 806 Izenberg, N. R., Arvidson, R. E., & Phillips, R. J. (1994). Impact crater degradation
807 on venusian plains. *Geophysical Research Letters*, *21*, 289-292. doi: 10.1029/
808 94GL00080
- 809 James, P. B., Zuber, M. T., & Phillips, R. J. (2013). Crustal thickness and support
810 of topography on venus. *Journal of Geophysical Research E: Planets*, *118*, 859-
811 875. doi: 10.1029/2012JE004237
- 812 Johnson, T. E., Brown, M., Kaus, B. J., & Vantongeren, J. A. (2014). Delamina-
813 tion and recycling of archaean crust caused by gravitational instabilities. *Na-
814 ture Geoscience*, *7*, 47-52. doi: 10.1038/ngeo2019
- 815 Katayama, I. (2021). Strength models of the terrestrial planets and implications
816 for their lithospheric structure and evolution. *Progress in Earth and Planetary
817 Science*, *8*. doi: 10.1186/s40645-020-00388-2
- 818 Katsura, T., Yamada, H., Shinmei, T., Kubo, A., Ono, S., Kanzaki, M., ... Utsumi,
819 W. (2003). Post-spinel transition in mg₂siO₄ determined by high p-t in situ
820 x-ray diffractometry. *Physics of the Earth and Planetary Interiors*, *136*, 11-24.
821 doi: 10.1016/S0031-9201(03)00019-0
- 822 Kay, R. W., & Kay, S. M. (1993). Delamination and delamination magmatism.
823 *Tectonophysics*, *219*, 177-189. doi: 10.1016/0040-1951(93)90295-U
- 824 Keskin, M. (2003). Magma generation by slab steepening and breakoff beneath a
825 subduction-accretion complex: An alternative model for collision-related vol-
826 canism in eastern anatolia, turkey. *Geophysical Research Letters*, *30*. doi:
827 10.1029/2003GL018019
- 828 King, S. (2018). Venus resurfacing constrained by geoid and topography. *Journal of
829 Geophysical Research: Planets*, *123*, 1041-1060. doi: 10.1002/2017JE005475
- 830 Kohlstedt, D. L., Evans, B., & Mackwell, S. J. (1995). Strength of the lithosphere:
831 constraints imposed by laboratory experiments. *Journal of Geophysical Re-
832 search*, *100*, 17587-17602. doi: 10.1029/95JB01460
- 833 Krystopowicz, N. J., & Currie, C. A. (2013). Crustal eclogitization and lithosphere
834 delamination in orogens. *Earth and Planetary Science Letters*, *361*, 195-207.
835 doi: 10.1016/j.epsl.2012.09.056

- 836 Li, Z. H., Liu, M., & Gerya, T. (2016). Lithosphere delamination in continental
 837 collisional orogens: A systematic numerical study. *Journal of Geophysical Re-*
 838 *search: Solid Earth*, *121*, 5186-5211. doi: 10.1002/2016JB013106
- 839 Lourenço, D. L., Rozel, A. B., Ballmer, M. D., & Tackley, P. J. (2020). Plutonic-
 840 squishy lid: A new global tectonic regime generated by intrusive magma-
 841 tism on earth-like planets. *Geochemistry, Geophysics, Geosystems*, *21*. doi:
 842 10.1029/2019GC008756
- 843 Mackwell, S. J., Zimmerman, M. E., & Kohlstedt, D. L. (1998). High-temperature
 844 deformation of dry diabase with application to tectonics on venus. *JOURNAL*
 845 *OF GEOPHYSICAL RESEARCH*, *103*, 975-984. doi: 10.1029/97JB02671
- 846 Magni, V., Faccenna, C., Hunen, J. V., & Funicello, F. (2013). Delamination vs.
 847 break-off: The fate of continental collision. *Geophysical Research Letters*, *40*,
 848 285-289. doi: 10.1002/grl.50090
- 849 Martin, P., Stofan, E. R., Glaze, L. S., & Smrekar, S. (2007). Coronae of parga
 850 chasma, venus. *Journal of Geophysical Research: Planets*, *112*. doi: 10.1029/
 851 2006JE002758
- 852 McKinnon, W. B., Zahnle, K. J., Ivanov, B. A., & Melosh, H. J. (1997). Crater-
 853 ing on venus - models and observations in bougher, s.w., huntent, d.m., and
 854 phillips, r.j., eds., venus ii geology, geophysics, atmosphere, and solar wind
 855 environment. , 969-1014.
- 856 Meissner, R., & Mooney, W. (1998). Weakness of the lower continental crust: a con-
 857 dition for delamination, uplift, and escape. *Tectonophysics*, *296*, 47-60. doi: 10
 858 .1016/S0040-1951(98)00136-X
- 859 Memiş, C., Göğüş, O. H., Şengül Uluocak, E., Pysklywec, R., Keskin, M., Şengör,
 860 A. M., & Topuz, G. (2020). Long wavelength progressive plateau uplift in east-
 861 ern anatolia since 20 ma: Implications for the role of slab peel-back and break-
 862 off. *Geochemistry, Geophysics, Geosystems*, *21*. doi: 10.1029/2019GC008726
- 863 Moresi, L., & Solomatov, V. (1998). Mantle convection with a brittle lithosphere:
 864 thoughts on the global tectonic styles of the earth and venus. *Geophysical*
 865 *Journal International*, *133*, 669-682. doi: 10.1046/j.1365-246X.1998.00521.x
- 866 Namiki, N., & Solomon, S. C. (1994). Impact crater densities on volcanoes and coro-
 867 nae on venus: Implications for volcanic resurfacing. *Science*, *265*, 929-933. doi:
 868 10.1126/science.265.5174.929

- 869 Nimmo, F., & McKenzie, D. (1997). Convective thermal evolution of the upper man-
 870 tles of earth and venus. *Geophysical Research Letters*, *24*, 1539-1542. doi: 10
 871 .1029/97GL01382
- 872 Ogawa, M., & Yanagisawa, T. (2014). Mantle evolution in venus due to magmatism
 873 and phase transitions: From punctuated layered convection to whole-mantle
 874 convection. *Journal of Geophysical Research: Planets*, *119*, 867-883. doi:
 875 10.1002/2013JE004593
- 876 O'Rourke, J. G., Wolf, A. S., & Ehlmann, B. L. (2014, 12). Venus: Interpreting the
 877 spatial distribution of volcanically modified craters. *Geophysical Research Let-*
 878 *ters*, *41*, 8252-8260. doi: 10.1002/2014GL062121
- 879 Parmentier, E. M., & Hess, P. C. (1992). Chemical differentiation of a convect-
 880 ing planetary interior: Consequences for a one plate planet such as venus. *Geo-*
 881 *physical Research Letters*, *19*, 2015-2018. doi: 10.1029/92GL01862
- 882 Perchuk, A. L., Safonov, O. G., Smit, C. A., van Reenen, D. D., Zakharov, V. S.,
 883 & Gerya, T. V. (2018). Precambrian ultra-hot orogenic factory: Mak-
 884 ing and reworking of continental crust. *Tectonophysics*, *746*, 572-586. doi:
 885 10.1016/j.tecto.2016.11.041
- 886 Petersen, R. I., Stegman, D. R., & Tackley, P. J. (2017). The subduction dichotomy
 887 of strong plates and weak slabs. *Solid Earth*, *8*, 339-350. doi: 10.5194/se-8-339
 888 -2017
- 889 Phillips, R. J., Arvidson, R. E., Boyce, J. M., Campbell, D. B., Guest, J. E., Sch-
 890 aber, G. G., & Soderblom, L. A. (1991). *Impact craters on venus: Initial*
 891 *analysis from magellan* (Vol. 252). doi: 10.1126/science.252.5003.288
- 892 Phillips, R. J., & Hansen, V. L. (1994). Tectonic and magmatic evolution of venus.
 893 *Annu. Rev. Earth Planet. Sci.*, *22*, 597-654. doi: 10.1146/annurev.ea.22.050194
 894 .003121
- 895 Phillips, R. J., & Izenberg, N. R. (1995). Ejecta correlations with spatial crater den-
 896 sity and venus resurfacing history. , *22*. doi: 10.1029/95GL01412
- 897 Phillips, R. J., Raubertas, R. F., Arvidson, R. E., Sarkar, I. C., Herrick, R. R., Izen-
 898 berg, N., & Grimm, R. E. (1992). Impact craters and venus resurfacing his-
 899 tory. *Journal of Geophysical Research*, *97*, 923-938. doi: 10.1029/92JE01696
- 900 Reese, C. C., Solomatov, V. S., & Moresi, L. N. (1999). Non-newtonian stagnant
 901 lid convection and magmatic resurfacing on venus. *Icarus*, *139*, 67-80. doi: 10

- 902 .1006/icar.1999.6088
- 903 Riedel, C., Michael, G. G., Orgel, C., Baum, C., van der Bogert, C. H., & Hiesinger,
904 H. (2021). Studying the global spatial randomness of impact craters on mer-
905 cury, venus, and the moon with geodesic neighborhood relationships. *Journal*
906 *of Geophysical Research: Planets*, *126*. doi: 10.1029/2020JE006693
- 907 Rolf, T., Steinberger, B., Sruthi, U., & Werner, S. C. (2018). Inferences on the
908 mantle viscosity structure and the post-overtun evolutionary state of venus.
909 *Icarus*, *313*, 107-123. doi: 10.1016/j.icarus.2018.05.014
- 910 Sandwell, D. T., & Schubert, G. (1992). Evidence for retrograde lithospheric sub-
911 duction on venus. *Science*, *257*, 766-770. doi: 10.1126/science.257.5071.766
- 912 Schaber, G. G., Strom, R. G., Moore, H. J., Soderblom, L. A., Kirk, R. L., Chad-
913 wick, D. J., ... Russell, I. (1992). Geology and distribution of impact craters
914 on venus: What are they telling us? *Journal of Geophysical Research: Planets*,
915 *97*, 257-270. doi: 10.1029/92JE01246
- 916 Schellart, W. P. (2010). Evolution of subduction zone curvature and its dependence
917 on the trench velocity and the slab to upper mantle viscosity ratio. *Journal of*
918 *Geophysical Research: Solid Earth*, *115*. doi: 10.1029/2009JB006643
- 919 Schellart, W. P., Freeman, J., Stegman, D. R., Moresi, L., & May, D. (2007). Evo-
920 lution and diversity of subduction zones controlled by slab width. *Nature*, *446*,
921 308-311. doi: 10.1038/nature05615
- 922 Schubert, G., & Sandwell, D. (1995). A global survey of possible subduction sites on
923 venus. *Icarus*, *117*, 173-196. doi: 10.1006/icar.1995.1150
- 924 Shalygin, E. V., Basilevsky, A. T., Markiewicz, W. J., Titov, D. V., Kreslavsky,
925 M. A., & Roatsch, T. (2012). Search for ongoing volcanic activity on venus:
926 Case study of maat mons, sapas mons and ozza mons volcanoes. *Planetary and*
927 *Space Science*, *73*, 294-301. doi: 10.1016/j.pss.2012.08.018
- 928 Shalygin, E. V., Markiewicz, W. J., Basilevsky, A. T., D.V.Titov, Ignatiev, N. I., &
929 Head, J. W. (2015). Active volcanism on venus in the ganiki chasma rift zone.
930 *Geophysical Research Letters*, *42*, 4762-4769. doi: 10.1002/2015GL064088
- 931 Shellnutt, J. G. (2016). Mantle potential temperature estimates of basalt from the
932 surface of venus. *Icarus*, *277*, 98-102. doi: 10.1016/j.icarus.2016.05.014
- 933 Smrekar, S. E., & Stofan, E. R. (1997). Corona formation and heat loss on venus by
934 coupled upwelling and delamination. *Science*, *277*(5330), 1289-1294.

- 935 Smrekar, S. E., Stofan, E. R., Mueller, N., Treiman, A., Elkins-Tanton, L., Helbert,
936 J., . . . Drossart, P. (2010). Recent hotspot volcanism on venus from virtis
937 emissivity data. *Science*, *328*, 605-608. doi: 10.1126/science.1186785
- 938 Solomon, S. C., Smrekar, S. E., Bindschadler, I. L. D., Grimm, R. E., Kaula, W. M.,
939 McGill, G. E., . . . Stofan, E. R. (1992). Venus tectonics: An overview of mag-
940 ellan observations. *Journal of Geophysical Research*, *97*(E8), 13,199-13,255.
941 doi: 10.1029/92JE01418
- 942 Stegman, D. R., Freeman, J., Schellart, W. P., Moresi, L., & May, D. (2006).
943 Influence of trench width on subduction hinge retreat rates in 3-d mod-
944 els of slab rollback. *Geochemistry, Geophysics, Geosystems*, *7*. doi:
945 10.1029/2005GC001056
- 946 Strom, R. G., Schaber, G. G., & Dawson, D. D. (1994). The global resurfacing of
947 venus. *Journal of Geophysical Research*, *99*, 899-909. doi: 10.1029/94JE00388
- 948 Tackley, P. J. (2008). Modelling compressible mantle convection with large
949 viscosity contrasts in a three-dimensional spherical shell using the yin-
950 yang grid. *Physics of the Earth and Planetary Interiors*, *171*, 7-18. doi:
951 10.1016/j.pepi.2008.08.005
- 952 Turcotte, D. L. (1993). An episodic hypothesis for venusian tectonics. *Journal of*
953 *Geophysical Research*, *98*, 61-78. doi: 10.1029/93JE01775
- 954 Turcotte, D. L. (1995). How does venus lose heat? *Journal of Geophysical Research*,
955 *100*, 16,931-16,940. doi: 10.1029/95JE01621
- 956 Turcotte, D. L., Morein, G., Roberts, D., & Malamud, B. D. (1999). Catastrophic
957 resurfacing and episodic subduction on venus. *Icarus*, *139*, 49-54. doi: 10
958 .1006/icar.1999.6084
- 959 Ueda, K., Gerya, T. V., & Burg, J. P. (2012). Delamination in collisional orogens:
960 Thermomechanical modeling. *Journal of Geophysical Research: Solid Earth*,
961 *117*. doi: 10.1029/2012JB009144
- 962 Uppalapati, S., Rolf, T., Cramer, F., & Werner, S. C. (2020). Dynamics of litho-
963 spheric overturns and implications for venus's surface. *Journal of Geophysical*
964 *Research: Planets*, *125*. doi: 10.1029/2019JE006258
- 965 Weller, M. B., & Kiefer, W. S. (2020). The physics of changing tectonic regimes:
966 Implications for the temporal evolution of mantle convection and the ther-
967 mal history of venus. *Journal of Geophysical Research: Planets*, *125*. doi:

968 10.1029/2019JE005960

969 Zuber, M. T. (1987). Constraints on the lithospheric structure of venus from
970 mechanical models and tectonic surface features. *Journal of Geophysical Re-*
971 *search*, *92*, E541-E551. doi: 10.1029/JB092iB04p0E541

972 Şengül Uluocak, E., Pysklywec, R. N., Göğüş, O. H., & Ulugergerli, E. U. (2019).
973 Multidimensional geodynamic modeling in the southeast carpathians: Up-
974 per mantle flow-induced surface topography anomalies. , *20*, 3134-3149. doi:
975 10.1029/2019GC008277